RESEARCH ARTICLE

Enhanced Signal Detection and Constellation Design for Massive SIMO Communications With 1-Bit ADCs

DOAA ABDELHAMEED[1,2], **(Student Member, IEEE), KENTA UMEBAYASHI**[1], **(Member, IEEE), ITALO ATZENI**[3], **(Member, IEEE), AND ANTTI TÖLLI**[3], **(Senior Member, IEEE)**

[1]Graduate School of Engineering, Tokyo University of Agriculture and Technology, Koganei-shi, Tokyo 184-8588, Japan
[2]Department of Electrical Engineering, Aswan University, Aswan 81528, Egypt
[3]Centre for Wireless Communications, University of Oulu, 90570 Oulu, Finland

Corresponding author: Doaa Abdelhameed (doaa-abdelhameed@st.go.tuat.ac.jp)

ABSTRACT In this paper, we investigate a transmitter and receiver design for a single-user massive SIMO (single-input multiple-output) system with 1-bit analog-to-digital converters (ADCs) at the base station (BS), where the user adopts higher-order modulation, e.g., 16-quadrature amplitude modulation (16-QAM), for the data transmission. For the channel estimation and the signal detection, linear least-squares (LS) estimation and maximum ratio combining (MRC) are respectively employed. In this context, we first introduce closed-form formulas for the mean of the estimated symbols and for the correlation matrix between their real and imaginary parts considering the effect of 1-bit quantization. The study of the distribution of the estimated symbols indicates that, in presence of 1-bit ADCs, the conventional 16-QAM detector and the typical square 16-QAM modulation are not adequate. In light of this, we propose three novel symbol detectors and re-design the 16-QAM modulation in order to improve the symbol error rate (SER). Furthermore, the upper bound on the SER is analyzed based on the pair-wise error probability and the boundary equation between two regions is also studied. Through numerical results, the proposed framework, i.e., the symbol detector and the transmit constellation design, shows a significant enhancement in the SER performance against the conventional detector and the typical square 16-QAM modulation.

INDEX TERMS Massive MIMO, 1-bit ADCs, data detection, upper bound on the SER, transmit constellation design.

I. INTRODUCTION

The fifth-generation (5G) (and beyond) mobile subscribers demand reliable communication systems providing immense data rates [1]. In this sense, the massive multi-input multi-output (MIMO) technology have attracted a great deal of attention due to its potential to improve both reliability and spectral efficiency [2]. Compared to conventional MIMO systems, the base station (BS) in the massive MIMO systems is equipped with a much larger number of antennas. Fully digital wide-bandwidth massive MIMO systems

The associate editor coordinating the review of this manuscript and approving it for publication was Taous Meriem Laleg-Kirati.

(with as many radio-frequency chains as antennas) come at the expense of considerable implementation challenges, such as enormous power consumption and hardware complexity [3].

The use of low-resolution analog-to-digital/digital-to-analog converters (ADCs/DACs) offer an auspicious settling for the practical impediments of the massive MIMO [4]. Employing the low-resolution ADC at the BS in the uplink can reduce the power consumption, as well as, the hardware complexity and the cost. Since the ADC's power consumption scales exponentially with its resolution, 1-bit ADCs can dramatically reduce the power consumption and the hardware complexity as it can be implemented using simple

comparators. Moreover, as the signal amplitude is clipped at the level of {1,-1}, the automatic gain control (AGC) is not required [5], [6] and power amplifiers with a small dynamic range can be used.

Numerous studies have been devoted to study merging the low-resolution and 1-bit ADCs with the communication systems [7], [8], [9], [10], [11], [12], [13], [14], [15], [16], [17], [18], [19], [20], [21], [22], [23], [24], [25], [26], [27], [28]. The system performance analysis is considered in [7], [8], [9], and [10]. In their respective works [7] and [8], the authors take the extreme case (1-bit) into account and examine the mutual information and achievable rate of the MIMO system. The low-resolution ADC scenario is studied in [9] and [10]. In [9], the symbol error rate (SER) performance for a single-input multi-output (SIMO) system with low-resolution ADCs is examined for the quadrature phase-shift keying (QPSK) signal in a Rayleigh fading channel. While the SER performance under the Nakagami-m fading channel is investigated in [10] for the M-ary pulse amplitude modulation (M-PAM) signal and the maximum likelihood (ML) detector at the receiver. For the capacity analysis, [11] studies the capacity of the massive MIMO system with low-resolution ADC under a real AWGN channel, while the case of the MIMO channel with correlated noise is considered in [12]. For flat fading channels, the capacity analysis of MIMO systems with 1-bit ADCs is presented in [13], assuming that the transmitter and receiver have complete knowledge of the channel state information. Moreover, the mm-wave MIMO channel capacity is analyzed in [14] for the high signal-to-noise ratio (SNR) regime utilizing 1-bit ADCs at the BS. Recently, a tight upper bound on the capacity of MIMO systems with 1-bit ADCs is introduced in [15] assuming AWGN channels. For systems with 1-bit ADCs, the channel estimation is explored in [16], [17], and [18]; for systems with few-bit ADCs, it is studied in [19] and [20]. In [16], the Bussgang decomposition is utilized to propose a channel estimation technique and obtain the achievable rate in a closed-form. The study in [17] exploits the Bussgang decomposition and oversampling to introduce a channel estimator for MIMO system with 1-bit ADCs. The channel estimation performance analysis under the unknown quantization threshold is introduced in [18]. The seminal paper [19] estimates the single-input single-output (SISO) channel with low precision ADCs, whereas [20] addresses the channel estimation for the massive MIMO orthogonal frequency division multiplexing (OFDM). The mm-wave MIMO channel estimation is investigated in [21] and [22] for 1-bit and low-resolution ADCs, respectively, at the BS. For the data detection in systems with low-resolution ADCs, one side of the literature tackles the case of 1-bit ADCs [23], [24], [25], [26], and the other side has been developed for few-bit ADCs [9], [20], [27], [28].

Despite the ADC nonlinearity, using simple linear signal processing (i.e., channel estimation and data detection) at the uplink quantized massive MIMO system receiver has gained a great interest in the literature [29], [30], [31], [32], [33], [34], [35], [36]. In [29], the authors provide an analytical expression for the conditional probability distribution and the mutual information closed-form expression of the estimated symbols for the uplink massive MIMO system with 1-bit ADCs. In this sense, a simple linear receiver, i.e., the standard linear least-squares (LS) channel estimation and the linear soft data estimation (maximum ratio combining (MRC) and zero-forcing (ZF)), is considered to estimate the QPSK symbols. The work in [30], [31], and [32] extends the analysis in [29] to the over-sampled MIMO system with 1-bit ADCs for the narrow band and the wideband channels. For the higher-order modulation case (16-quadrature amplitude modulation (16-QAM)), as an extension to [29], the study in [33] analyzes the system performance for a flat fading channel and shows that LS channel estimation and MRC at the BS are sufficient for the 16-QAM symbols to be detectable after the 1-bit quantization under the conditions that the BS equipped with a massive number of antennas and in the presence of the random noise. This phenomenon (i.e., constructive noise phenomenon) is also observed in [37], and previously mentioned in [38] as a stochastic resonance phenomenon. Recently, the investigations in [34] continue the state-of-the-art by providing the closed-form expression for the channel estimation mean squared error (MSE) for both LS and minimum MSE estimators. Subsequently, the analytical expressions for the mean and the variance are obtained with MRC soft estimation when 1-bit ADCs are adopted. For the low-resolution ADCs combined with the linear receiver, [35], [36] extends the work in [29] and [33]. In [35], the bit error rate (BER) performance utilizing the additive quantization noise model (AQNM) [39] is analyzed for the uniform and the non-uniform quantization. While [36] considers the Bussgang decomposition [40] to propose a channel estimator, building on this estimator, achievable rate approximation is as well obtained.

In this paper, we consider the uplink massive SIMO system with 1-bit ADCs connected to the BS, i.e., 1-bit ADC for each component of the received signal. Furthermore, we assume a higher-order modulation (e.g., 16-QAM) is used in combination with a simple linear receiver (i.e., LS channel estimator and normalized MRC symbol estimation). First, we derive the statistics of the estimated symbols and appropriate symbol detectors. Then, a transmit constellation symbols design is proposed to enhance the SER performance based on the statistical analysis. Specifically, the contributions are summarized as follows:

- For the uplink massive SIMO system with 1-bit ADCs, we obtain the mean of the estimated symbol and the covariance and/or correlation matrix between the real and imaginary parts of the estimated symbol. According to that, the distribution of the estimated symbol is introduced and its oval shape in the I-Q plane is described.
- Utilizing the statistics of the estimated symbol, we investigate three statistical-based symbol detectors.[1] The first

---

[1]This contribution extends the work in [41] by considering the statistical analysis, while the third detector and the other contributions are being put forth for the first time.

detector is designed based on only the mean of the estimated symbols, while the second one utilizes the mean and variance for symbol detection since each constellation point has a different variance. For more compensation for the effects of 1-bit ADCs, the mean and the covariance matrix are considered in the last detector.

- Finally, we derive an analytical expression for the upper bound on the SER by considering the pair-wise error probability. Based on a proposed metric and the upper bound on the SER, a transmit constellation symbols design is also proposed in order to improve the SER performance. In this sense, a pre-compensation to the 1-bit quantization distortion, i.e., the symbol overlapping, is considered by selecting a proper transmit constellation design.

Outline: The remainder of the paper is structured as follows. First, Section II presents the system model and the problem formulation considered in this paper. Section III provides our system analysis, the proposed symbol detectors, and the corresponding numerical results. The upper bound on the SER is introduced in Section IV as well as the dedicated numerical results. Section V introduces the transmit constellation symbols design approach and the related numerical results. Finally, Section VI concludes and summarizes our paper.

Notation: The following notation is considered throughout the paper. The boldface uppercase and lowercase letters is used for matrices and vectors, respectively, while the italic uppercase and lowercase refer to scalar, i.e., A, a. $r_{a,b}$ is the (a, b)th element of matrix $\mathbf{R}$, while, r_a represent the ath element of a vector $\mathbf{r}$. $\Re(\cdot)$ and $\Im(\cdot)$ refer to the complex number parts real and imaginary, respectively. sgn$(\cdot)$ refers to the element-wise signum function. $\mathcal{CN}(\mu, \sigma^2)$ refers to the circularly symmetric complex Gaussian random variable with a complex mean μ and variance σ^2, while $\mathcal{N}(\mu_R, \sigma_R^2)$ is the real normal random variable with mean μ_R and variance σ_R^2, and $\mathcal{N}_n(\boldsymbol{\mu}, \boldsymbol{\Sigma})$ denotes the n-variate random variable with mean vector $\boldsymbol{\mu} \in \mathbb{C}^{n \times 1}$ and covariance matrix $\boldsymbol{\Sigma} \in \mathbb{C}^{n \times n}$. $\mathbb{E}[\cdot]$ denotes the mean operator. Lastly, $(\cdot)^H$, $(\cdot)^*$, and $(\cdot)^T$ denote the Hermitian transpose, conjugate, and transpose operators, respectively, whereas $\mathbf{I}$ represents the identity matrix.

II. SYSTEM MODEL AND PROBLEM FORMULATION

A single-cell uplink massive-scale SIMO system, depicted in Figure 1, is considered in this paper. In such system, M antennas are equipped at the BS to serve a single-antenna user (UE). A block Rayleigh fading channel is assumed, where $\mathbf{h}$ represents the uplink channel vector between the UE and the BS. The entries of $\mathbf{h}$ are independent and identically distributed (i.i.d.) as $h_m \sim \mathcal{CN}(0, 1)$. At the BS, each radio-frequency chain includes two 1-bit ADCs to independently quantize the in-phase and the quadrature-phase components i.e., $2M$ ADCs are needed. The quantization function is given by

$$Q(z) = \text{sgn}\left(\Re(z)\right) + j\,\text{sgn}\left(\Im(z)\right). \quad (1)$$

There are two phases: channel estimation phase and data transmission phase and $\mathbf{h}$ is assumed to be constant during the two phases. In the following sections, detailed procedures in the two phases are shown.

A. CHANNEL ESTIMATION

In the phase of the channel estimation, the UE transmits a pilot sequence $\mathbf{x}$ with length P to estimate the channel vector in the uplink transmission. We assume the UE pilot sequence $\mathbf{x} \in \mathbb{C}^{1 \times P}$ is drawn from a higher-order modulation (e.g., the typical square 16-QAM). At the BS, the baseband received pilot signal matrix is given by

$$\mathbf{Y}_P = \mathbf{h}\mathbf{x} + \mathbf{N}_P \quad (2)$$

where, $\mathbf{Y}_P \in \mathbb{C}^{M \times P}$, $\mathbf{N}_P \in \mathbb{C}^{M \times P}$ denotes the AWGN matrix and the entries of AWGN matrix are distributed as $\mathcal{CN}(0, \sigma_n^2)$. Hence, the transmit SNR is equal to $\frac{1}{\sigma_n^2}$ with a unit average transmit power. Then, the quantized received pilots is given by

$$\mathbf{R}_P = Q(\mathbf{Y}_P). \quad (3)$$

For the channel vector estimation, we assume a standard LS estimation as in [29]. The estimated channel response is given by

$$\hat{\mathbf{h}} = \underset{\tilde{\mathbf{h}}}{\arg\min} \|\mathbf{R}_P - \tilde{\mathbf{h}}\mathbf{x}\| \quad (4)$$

$$= \left(\mathbf{x}\mathbf{x}^H\right)^{-1} \mathbf{R}_P \mathbf{x}^H. \quad (5)$$

B. DATA TRANSMISSION

In the uplink transmission, a static channel response during the coherence interval is assume. Let the transmit SNR be the same for the two transmission phases. Then the received signal vector $\mathbf{y}_d \in \mathbb{C}^{M \times 1}$ at the BS is expressed as

$$\mathbf{y}_d = \mathbf{h}s + \mathbf{n}_d \quad (6)$$

where $\mathbf{n}_d$ represents the AWGN vector, and s denotes the UE complex data symbol, which is drawn from the same constellation as the pilot signal (e.g., square 16-QAM). In this paper, the number of modulation levels used is assumed to be 16 without loss of generality, i.e., $s \in \mathbf{s}$ and $\mathbf{s} = [s_1, \cdots, s_{16}]^T$. However, it can be extended to any number of modulation levels, $\mathbf{s} \in \mathbb{C}^{K \times 1}$. The quantized version of the received signal $\mathbf{y}_d$ is expressed as

$$\mathbf{r}_d = Q(\mathbf{y}_d). \quad (7)$$

The MRC estimated signal s_{soft}, based on the standard LS estimation (4), can be calculated as

$$s_{\text{soft}} = \frac{\hat{\mathbf{h}}^H \mathbf{r}_d}{\|\hat{\mathbf{h}}\|^2} \quad (8)$$

where $\frac{\hat{\mathbf{h}}}{\|\hat{\mathbf{h}}\|^2}$ is the combining vector [29]. A detector at the receiver detects the transmit symbol $s \in \mathbf{s}$ based on s_{soft}.
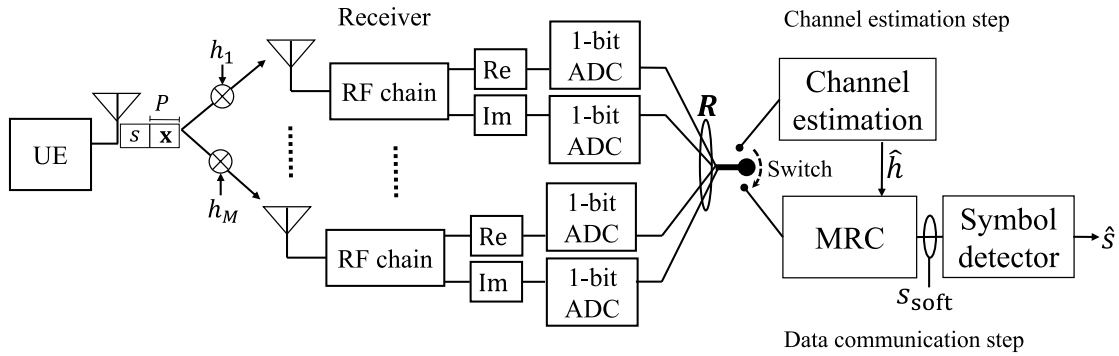
FIGURE 1. Uplink massive SIMO system model.

In the conventional detector for the typical square 16-QAM constellation, the detection result $\hat{s}$ is given by

$$\hat{s} = \underset{s_k \in \mathbf{s}}{\arg\min} |s_k - s_{\text{soft}}| \tag{9}$$

where s_k belongs to the typical square 16-QAM constellation points, i.e., $\mathbf{s} = \frac{1}{\sqrt{10}}\{\pm 3 \pm j3, \pm 3 \pm j1, \pm 1 \pm j3, \pm 1 \pm j1\}$, which is normalized such that $\frac{1}{K}\sum_{k=1}^{K}|s_k|^2 = 1$. In the proposed detectors, we consider the statistics of s_{soft} to design the signal detection metrics. Furthermore, in the proposed transmit symbol design, s_k in the I-Q plane is also designed based on the estimated symbols statistics.

III. SYMBOL ANALYSIS AND DATA DETECTION

In this section, at first the statistics of s_{soft} for a given arbitrary transmit symbol $s \in \mathbf{s}$ are derived in Section III-A. After that, in Section III-B, the proposed symbol detectors are presented.

A. ESTIMATED SYMBOL ANALYSIS

The authors in [34] introduced the statistical characteristics of the estimated symbol by giving the closed-form expressions for the symbol mean and variance. On the one hand, the authors assumed a special pilot sequence as well as utilized a non-optimal MRC estimator. On the other hand, [34] considered the estimated symbol as normally distributed complex random variable with uncorrelated components, i.e., circular symmetric complex Gaussian random variable. So, we fill this gap by investigating general (i.e., applicable for any pilot sequence) closed-form formulas of the mean value and the variance when the optimal MRC (8) estimates the symbols. In addition, the covariance and/or the correlation matrix between the real and imaginary parts of the estimated symbol are investigated, which have not been touched in the literature. Finally, by utilizing the statistics of the estimated symbols, we provide the symbol distribution and explain its behavior. By plugging (4) into (8), the MRC soft estimation can be rewritten as

$$s_{\text{soft}} = P\frac{\mathbf{x}\mathbf{R}_{\text{P}}^H \mathbf{r}_d}{\mathbf{x}\mathbf{R}_{\text{P}}^H \mathbf{R}_{\text{P}}\mathbf{x}^H}. \tag{10}$$

Theorem 1: For a transmit symbol s, the approximated mean value of the estimated symbol s_{soft} in (10), $\mu_s \approx \mathbb{E}[s_{\text{soft}}]$, is calculated as

$$\mu_s = \frac{P\sum_{p=1}^{P} x_p \left(\Omega\left(\rho_{\text{RR}}^{(x_p,s)}\right) + j\,\Omega\left(\rho_{\text{RI}}^{(x_p,s)}\right)\right)}{P + \sum_{p\neq u} x_p x_u^* \left(\Omega\left(\rho_{\text{RR}}^{(x_p,x_u)}\right) + j\,\Omega\left(\rho_{\text{RI}}^{(x_p,x_u)}\right)\right)} \tag{11}$$

with

$$\Omega(a) = \frac{2}{\pi}\arcsin(a), \tag{12}$$

$$\rho_{\text{RR}}^{(x,y)} = \frac{\Re(x^*y)}{\eta_{xy}}, \tag{13}$$

$$\rho_{\text{RI}}^{(x,y)} = \frac{\Im(x^*y)}{\eta_{xy}}, \tag{14}$$

$$\eta_{xy} = \sqrt{\left(|x|^2 + \frac{1}{\text{SNR}}\right)\left(|y|^2 + \frac{1}{\text{SNR}}\right)}. \tag{15}$$

Proof: See Appendix A. $\square$

Theorem 2: Let $\mu_{\text{R}_s} = \Re(\mu_s)$ and $\mu_{\text{I}_s} = \Im(\mu_s)$. Furthermore, let v_{R} and v_{I} denote the real and imaginary parts of s_{soft}, respectively, when s is transmitted. The covariance matrix of $[v_{\text{R}}\ v_{\text{I}}]^T$ can be approximated as

$$\Sigma_s = \begin{bmatrix} \sigma_{\text{R}_s}^2 & \sigma_{\text{RI}_s}^2 \\ \sigma_{\text{RI}_s}^2 & \sigma_{\text{I}_s}^2 \end{bmatrix} \tag{16}$$

with

$$\sigma_{\text{R}_s}^2 = \frac{MP^2}{\Xi}(2P + 2\xi_1 + 2\xi_2 + \xi_3) \\ - \frac{M\Xi - (M-1)E^2}{M\Xi}\mu_{\text{R}_s}^2, \tag{17}$$

$$\sigma_{\text{I}_s}^2 = \frac{MP^2}{\Xi}(2P + 2\xi_1 - 2\xi_2 - \xi_3) \\ - \frac{M\Xi - (M-1)E^2}{M\Xi}\mu_{\text{I}_s}^2, \tag{18}$$

$$\sigma_{\text{RI}_s}^2 = \frac{MP^2}{\Xi}(2\bar{\xi}_1 + 4\bar{\xi}_2 + \bar{\xi}_3) \\ - \frac{M\Xi - (M-1)E^2}{M\Xi}\mu_{\text{R}_s}\mu_{\text{I}_s} \tag{19}$$

and

$$E = \mathbb{E}\left[\mathbf{x}\mathbf{R}_P^H\mathbf{R}_P\mathbf{x}^H\right], \tag{20}$$

$$\Xi = \mathbb{E}\left[\left(\mathbf{x}\mathbf{R}_P^H\mathbf{R}_P\mathbf{x}^H\right)^2\right] \tag{21}$$

where the expressions of ξ_1, ξ_2, ξ_3, $\bar{\xi}_1$, $\bar{\xi}_2$, and $\bar{\xi}_3$ are in (98)–(103), as shown at the bottom of page 15, while E is obtained as in (85) and Ξ is given with the procedure mentioned in Appendix B. The mean of a quadrivariate normally distributed random variable, which appears in ξ_2, ξ_3, $\bar{\xi}_2$, $\bar{\xi}_3$, and Ξ expressions, is only calculated numerically, while the rest of the equations are given in closed-form formulas.

Proof: See Appendix B. □

From (17)–(19), the approximated correlation coefficient between the real and imaginary components of s_{soft} is given by

$$\rho_s = \frac{\sigma_{\text{RI}_s}^2}{\sqrt{\sigma_{\text{R}_s}^2 \sigma_{\text{I}_s}^2}} \tag{22}$$

and the approximated variance of the estimated symbol s_{soft} is given by

$$\sigma_s^2 = \sigma_{\text{R}_s}^2 + \sigma_{\text{I}_s}^2 \tag{23}$$

$$= \frac{4MP^2}{\Xi}(P + \xi_1) - \frac{M\Xi - (M-1)E^2}{M\Xi}|\mu_s|^2. \tag{24}$$

In the literature [29], [34], the authors considered the estimated symbol, when 1-bit ADCs are used at the BS, as a complex normally distributed random variable with uncorrelated in-phase and quadrature-phase components, i.e., $s_{\text{soft}} \sim \mathcal{CN}(\mu_s, \sigma_s^2)$, which is the case of the full-resolution system. In addition, [33] and [34] numerically demonstrated the non-symmetric shape of the distribution of the estimated symbols in the I-Q plane. However, the explanation behind this behaviour was not provided. In this regard, we bridge this gap in the existing literature by utilizing the covariance matrix derived in Theorem 2 to characterize the estimated symbols distribution.

Corollary 1: Given the expressions (11) and (16), the estimated symbols of the massive SIMO system, with 1-bit ADCs, LS channel estimation, and MRC at the receiver, can be shown to be distributed as

$$\mathbf{s}_{\text{soft}} = \left[\Re(s_{\text{soft}})\ \Im(s_{\text{soft}})\right]^T \tag{25}$$

$$\sim \mathcal{N}_2(\boldsymbol{\mu}_s, \boldsymbol{\Sigma}_s) \tag{26}$$

with

$$\boldsymbol{\mu}_s = [\mu_{\text{R}_s}\ \mu_{\text{I}_s}]^T \tag{27}$$

where $\sigma_{\text{RI}_s}^2 \neq 0$.

Proof: See Appendix C. □

The investigation in Corollary 1 identifies the distribution of the estimated symbols and enables us to clarify the different dispersion around the mean, especially in the high SNR regime.
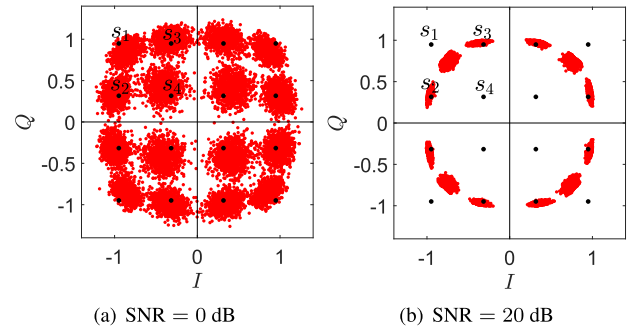

(a) SNR = 0 dB (b) SNR = 20 dB

FIGURE 2. Estimated symbols in the I-Q plane for different SNR values, with $P = 256$ and $M = 100$.

B. PROPOSED SYMBOL DETECTORS

Figure 2 shows the transmit symbols (black dots) $s_k \in \mathbf{s}$, i.e., the typical square 16-QAM constellation and the dedicated estimated symbols (red dots) in the I-Q plane in low (i.e., 0 dB) and high (i.e., 20 dB) SNR. In this figure, a $P = 256$ pilot sequence is used, and 100 antennas are connected at the BS. It is noted from Figure 2 that the statistics of the estimated symbols in the 1-bit ADCs scenario are different from the full-resolution case. On the one hand, the mean of the estimated symbol depends on the SNR. On the other hand, each estimated symbol shows different variance and distribution. So, investigating new symbol detectors that use the estimated symbol statistics is therefore essential.

1) MEAN-BASED DETECTOR

Let μ_{s_k} be the mean of the estimated symbol at the MRC when s_k is transmitted. In the SIMO system with 1-bit ADCs, μ_{s_k} is not equal to s_k as shown from Figure 2. The proposed mean-based symbol detector exploits the mean to detect the symbols as

$$\hat{s} = \underset{s_k \in \mathbf{s}}{\arg\min}|s_{\text{soft}} - \mu_{s_k}| \tag{28}$$

and μ_{s_k} is evaluated from (11).

2) MEAN AND VARIANCE-BASED DETECTOR

It is obvious from Figure 2 that not only the mean but also the variance of s_{soft} depend on s_k. In the proposed mean and variance-based detector, both the mean and the variance are considered for the detection as

$$\hat{s} = \underset{s_k \in \mathbf{s}}{\arg\min}\frac{|s_{\text{soft}} - \mu_{s_k}|}{\sqrt{\sigma_{s_k}^2}} \tag{29}$$

with $\sigma_{s_k}^2$ is the approximated variance when s_k is transmitted, and is calculated from (24).

3) MEAN AND COVARIANCE-BASED DETECTOR

In this section, the mean and covariance-based detector is investigated not only to consider the mean and the variance variation but also the dispersion around the mean and the symbol orientation. In this regard, the received symbol is mapped to the closest reference by utilizing the covariance
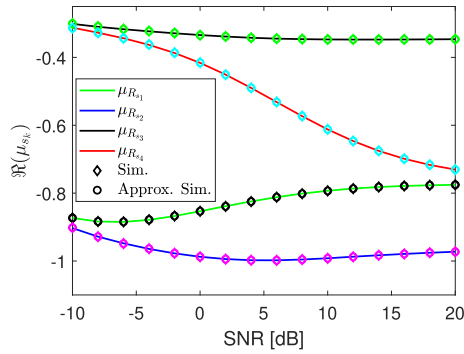
(a) Real part
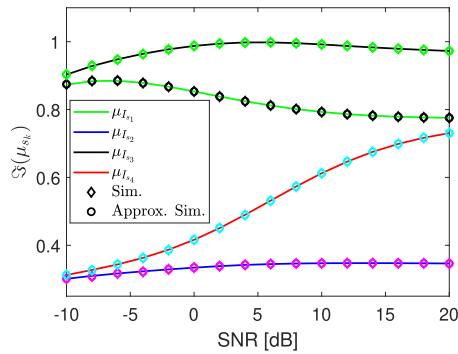
(b) Imaginary part

FIGURE 3. Mean value μ_k versus the SNR, with $P = 256$ and $M = 100$.
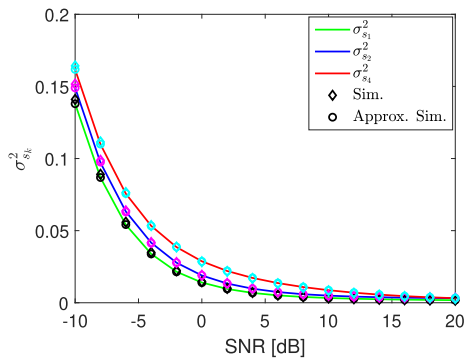

FIGURE 4. Variance of the estimate symbols versus the SNR, with $P = 256$ and $M = 100$.

matrix in orientating the symbol according to the candidate references as

$$\hat{s} = \underset{k}{\arg\min}|\bar{s}_k - \mu_{s_k}| \tag{30}$$

where $\bar{s}_k$ is given by

$$\bar{s}_k = \ddot{s}_1 + j\ddot{s}_2, \tag{31}$$

with

$$\ddot{s} = \sqrt{\frac{\sigma_{s_k}^2}{2}} \mathbf{U}_{s_k}^{-1} \mathbf{s}_{\text{soft}} + \left(\mathbf{I}_2 - \sqrt{\frac{\sigma_{s_k}^2}{2}} \mathbf{U}_{s_k}^{-1} \right) \boldsymbol{\mu}_{s_k}, \tag{32}$$

$$\boldsymbol{\mu}_{s_k} = \begin{bmatrix} \Re(\mu_{s_k}) & \Im(\mu_{s_k}) \end{bmatrix}^T \tag{33}$$

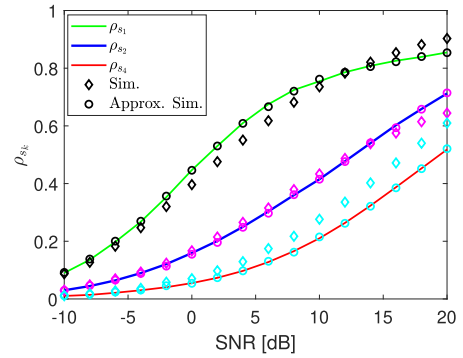**FIGURE 5.** Correlation between the real and imaginary components of the estimated symbols versus the SNR, with $P = 256$ and $M = 100$.
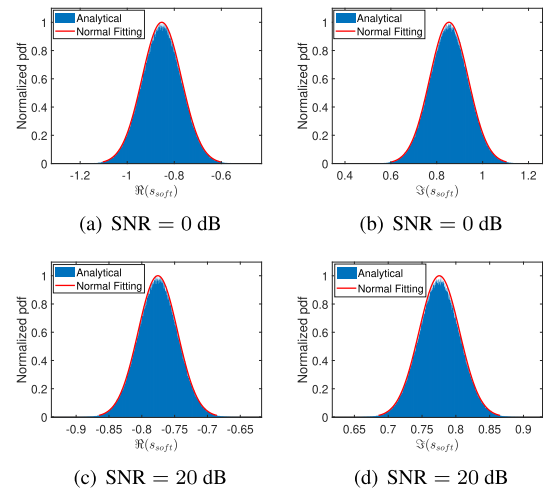

(a) SNR = 0 dB

(b) SNR = 0 dB

(c) SNR = 20 dB

(d) SNR = 20 dB

FIGURE 6. Distribution of the real and imaginary parts of s_1, with $P = 256$ and $M = 100$.

where $\ddot{\mathbf{s}} \in \mathbb{C}^{2 \times 1}$ contains the rotated symbol components, and $\mathbf{U}_{s_k}$ refers to the lower triangular matrix of the Cholesky decomposition of the covariance matrix of symbol s_k, i.e.,

$$\Sigma_{s_k} = \mathbf{U}_{s_k} \mathbf{U}_{s_k}^* \tag{34}$$

with Σ_{s_k} computed as in (16).

C. NUMERICAL RESULTS

In this section, we verify the statistical analysis introduced in Section III-A and examine the proposed symbol detectors. Through this section, the numerical results are obtained by utilizing the closed-form formulas in (11), (16-19), (22), and (24), if nothing else is mentioned. The transmit symbols in the two communication phases, i.e., channel estimation and data transmission, are selected from the typical square 16-QAM symbols. However, the statistical analysis and the proposed symbol detectors are applicable for any set of transmit symbols. Lastly, the pilot design is considered as a repetition of the 16-QAM symbols.

In Figures 3–5, we examine the statistical analysis by comparing it with the Monte Carlo simulations (Sim.) and the Monte Carlo simulations when considering the
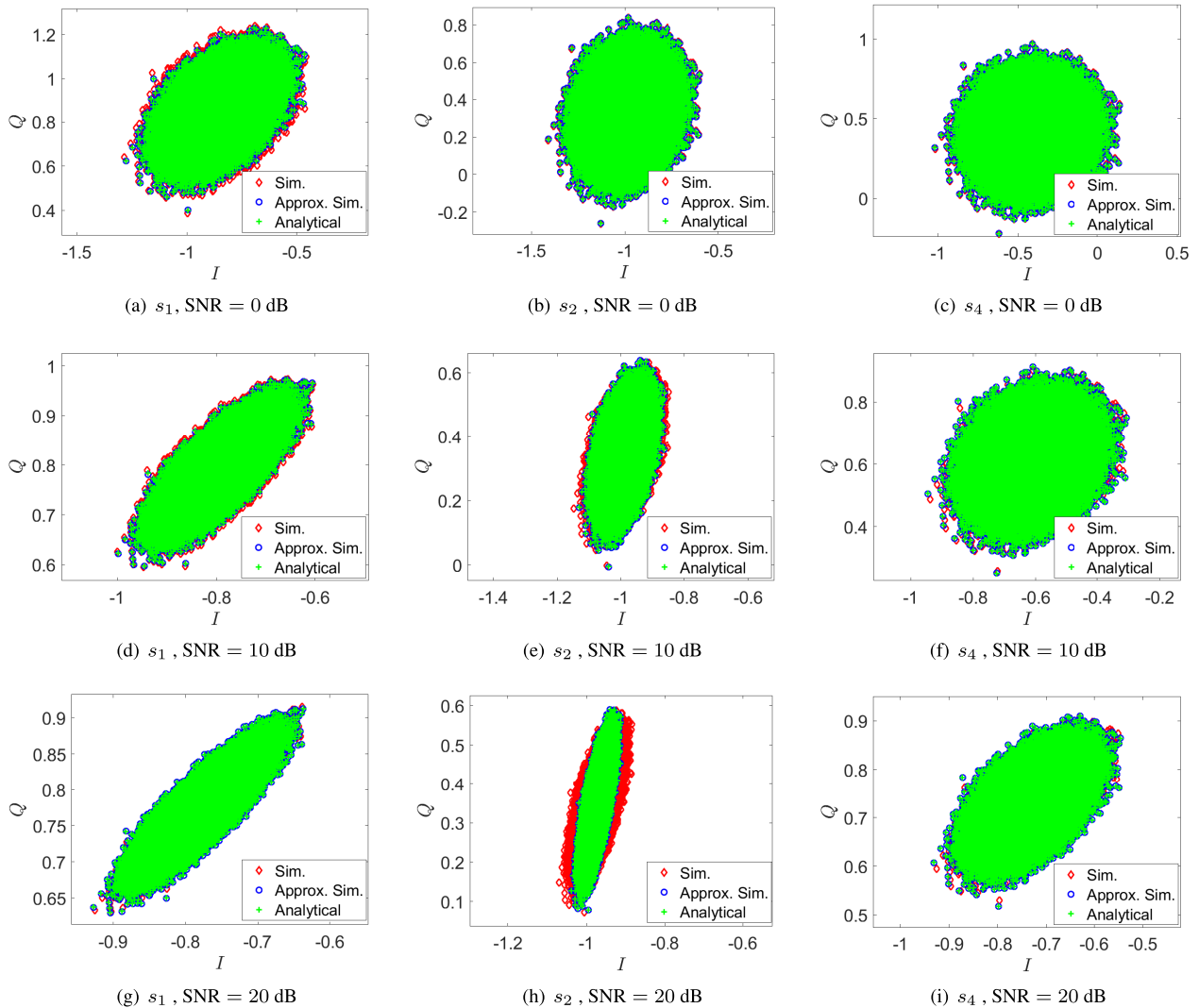
FIGURE 7. Estimated symbols distribution in the I-Q plane, with *P* = 256 and *M* = 100.

approximation assumed in Theorem 1 (69) (Approx. Sim.), i.e., by obtaining the right hand side of (70) and (86)–(88) numerically to verify the suggested approximation, for the typical square 16-QAM symbols shown in Figure 2. The aforementioned figures consider $M = 100$ and $P = 256$, and the simulation is obtained by averaging over 10^5 independent channel realizations. Figures 3(a) and (b) validate the real and imaginary mean of the estimated symbols obtained from (11), respectively. From the variance point of view, Figure 4 proves the validation of the approximation in the variance analysis with different SNR. Figure 5 shows the correlation coefficient between the real and imaginary components of the estimated symbol. Unlike the massive SIMO system with the full-resolution ADCs, this figure shows that the correlation between the in-phase and the quadrature-phase components of the estimated symbol increases with the SNR. At high SNR, we notice a slight difference in the correlation coefficient between the analysis and the Monte Carlo

simulations (Sim.), which will be shown to be negligible in terms of the SER performance.

To validate the model considered in Corollary 1 for the estimated symbols, Figures 6 and 7 are provided. Figure 6 shows the distribution, which are obtained from the analysis, and the normal fitting for the estimated symbol related to s_1. Figures 6(a) and (b) introduce the case of low SNR, i.e., SNR = 0 dB for the real and imaginary components, respectively. While the high SNR scenario, i.e., SNR = 20 dB, is provided in Figures 6(c) and (d). Through the above-mentioned plots, the separate distributions of the estimated symbol components fit the normal distribution in the low and high SNR regions, which validate the assumption that s_{soft} is normally distributed (26). In Figure 7, the distribution of the estimated symbols for a given transmit symbol s_k in the I-Q plane is shown. For the validation, the symbols generated empirically from the simulations are considered, i.e., Sim. and Approx Sim. The figure consists of a
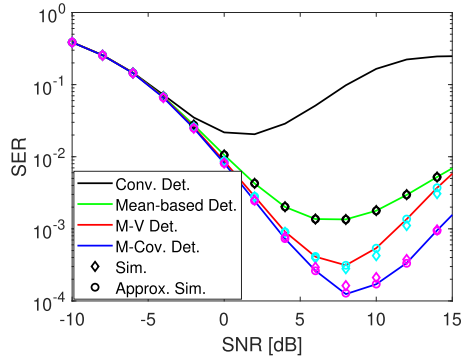
FIGURE 8. SER versus the SNR for the conventional detector and the proposed symbol detectors, with $P = 256$ and $M = 100$.
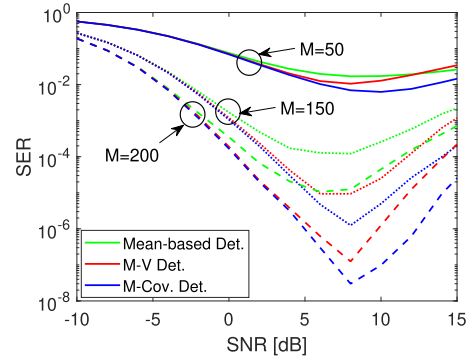

FIGURE 9. SER versus the SNR for the proposed symbol detectors, with $M = 100$ and different values of P.
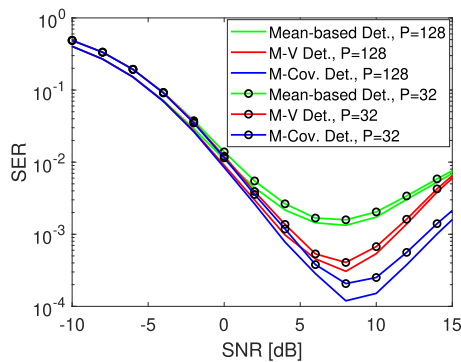

FIGURE 10. SER versus the SNR for the proposed symbol detectors, with $P = 256$ and different values of M.

3×3 grid, the different rows refer to different SNRs, while the columns are associated to different transmit signal s_k. Figures 7(a), (d), and (g) show the distribution of the estimated symbol when s_1 has been transmitted for SNR = 0, 10, and 20 dB respectively. Increasing the SNR leads to an increase in the sharpness of the oval shape of the distribution, which is a translation to the increasing in the correlation between the I and Q components. On the other hand, the case of s_4 (Figures 7(c), (f), and (i)), which is more likely to be affected by the noise, shows a wider distribution, which means less correlation coefficient. For instance, the distribution in Figure 7(c) tends to be a circle, which is the case of independent random variables in the low SNR case such as SNR = 0 dB. This behavior can also be confirmed from Figure 5. For s_1 and s_4, the considered approximation matches the actual distribution regardless of the slight difference in the correlation shown in Figure 5. In s_2 case, the difference in the I-Q plane distribution between the simulation and analysis in Figure 7(h) (20 dB) results from the difference mentioned in Figure 5. The results in Figure 7 highlight the benefits of our contribution in considering the covariance matrix of the estimated symbols in describing their distributions.

Figure 8 shows the SER versus the SNR for $P = 256$ and $M = 100$. In this result, we show the SER performance of the three proposed detectors: the mean-based detector

(Mean-based Det.), the mean and variance-based detector (M-V Det.), and the mean and covariance-based detector (M-Cov. Det.), in addition to the SER performance of the conventional detector (Conv. Det.) for comparison. To verify the approximation assumed in Theorem 1 (69), the SER obtained from the Monte Carlo simulations is also added (Sim. and Approx. Sim.). For the proposed three detectors, the approximation considered in Theorem 1 (69) fits the Monte Carlo SER, which validates the assumption and emphasizes that the difference in the correlation showed in Figure 5 between the theoretical and the Sim. does not affect on the averaged SER performance. The investigated three detectors significantly enhance the SER performance compared with the conventional one. The performance gap between the conventional and mean-based detectors shows the value behind using μ_{s_k} as a reference point instead of the transmit symbol. Considering the variance σ_s^2 in the mean and variance-based symbol detector reduces the SER over the one obtained from the mean-based symbol detector. Lastly, the SER performance gain between the mean and covariance-based symbol detector and the other detectors shows the benefits of using the covariance matrix in detecting the signal.

Figures 9 and 10 give the SER performance of the suggested detectors against the SER for different system setups. Figure 9 examines the detectors performance with 100 antennas and different pilot sequence lengths, i.e., 32, 128. Still, the mean and covariance detector shows the lowest SER among the proposed detectors in 32 and 128 pilot sequence cases. On the other hand, Figure 10 considers a $P = 256$ pilot sequence and different number of antennas. Increasing the number of antennas, i.e., from 50 to 200, enhances the SER performance.

For all methods and setups, the SER curves show that the massive SIMO with 1-bit ADCs obtains optimum SNRs where the performance can be minimized. These SNR values vary based on the system parameters and the system detectors as well. However, the performance indicates that the constellation of the typical square 16-QAM is not suitable for the massive SIMO with 1-bit ADCs. Therefore, in Section V, we will consider designing a suitable signal constellation.

IV. THE UPPER BOUND ON THE SYMBOL ERROR RATE ANALYSIS

In this section, we focus on the SER analysis to characterize the performance of the massive SIMO system with 1-bit ADCs when the mean and variance-based detector is considered. In this respect, the detection boundaries between the different regions are illustrated by considering the pairwise detection. Then, building on that, the upper bound on the SER is investigated.

A. DETECTION BOUNDARIES

To investigate the detection boundaries, at first, we introduce the pair-wise detector where a set of only two symbols constellation $s_{pw} = \{s_l, s_w\}$ is assumed, where $l \neq w$ and $l, w \in \mathcal{K} = \{1, 2, \ldots, K\}$., The pair-wise detector rule, which follows the mean and variance-based detector, is given by

$$\hat{s}_{pw} = \underset{s_i \in s_{pw}}{\operatorname{argmin}} \frac{|s_{soft} - \mu_{s_i}|}{\sqrt{\sigma_{s_i}^2}}. \tag{35}$$

In this sense, the I-Q plane can be divided into two regions denoted by $\gamma_w^{(l)}$ and $\gamma_l^{(w)}$, which are defined as

$$\gamma_a^{(b)} = \{s_{soft} \in \mathcal{F} : d(s_{soft}, s_a) \leq d(s_{soft}, s_b)\}, \quad b \in \mathcal{K}_a \tag{36}$$

with

$$\mathcal{K}_a = \{b \in \mathcal{K} : b \neq a\}, \tag{37}$$

$$\mathcal{F} = \bigcup_{w=1}^{K} \gamma_w, \tag{38}$$

$$\gamma_w = \bigcap_{l \in \mathcal{K}_w} \gamma_w^{(l)} \tag{39}$$

$$= \{s_{soft} \in \mathcal{F} : d(s_{soft}, s_w) \leq d(s_{soft}, s_l), l \in \mathcal{K}_w\}, \quad w \in \mathcal{K} \tag{40}$$

where $d(\cdot, \cdot)$ refers to the scaled Euclidean distance (ED) considered in the mean and variance-based symbol detector (29), γ_w refers to the detection region related to the symbol s_w, i.e., results from detector (29), and $\gamma_w^{(l)}, \gamma_l^{(w)}$ denote the pair-wise detection regions, i.e., considering detector (35).

Theorem 3: Let $(\acute{x}, \acute{y})$ denote point coordinates in the I-Q plane, and are located on the boundary ϖ_{lw} between the two regions $\gamma_w^{(l)}$ and $\gamma_l^{(w)}$, satisfy the following equations

$$c_1\acute{x}^2 + c_1\acute{y}^2 - c_2\acute{x} - c_3\acute{y} - c_4 = 0 \tag{41}$$

with

$$c_1 = \sigma_{s_l}^2 - \sigma_{s_w}^2, \tag{42}$$

$$c_2 = 2\left(\Re\left(\mu_{s_w}\right)\sigma_{s_l}^2 - \Re\left(\mu_{s_l}\right)\sigma_{s_w}^2\right), \tag{43}$$

$$c_3 = 2\left(\Im\left(\mu_{s_w}\right)\sigma_{s_l}^2 - \Im\left(\mu_{s_l}\right)\sigma_{s_w}^2\right), \tag{44}$$

$$c_4 = \sigma_{s_w}^2|\mu_{s_l}|^2 - \sigma_{s_l}^2|\mu_{s_w}|^2. \tag{45}$$

Proof: See Appendix D. □

The result in Theorem 3 indicates that the boundary between two regions $\gamma_w^{(l)}, \gamma_l^{(w)}$ follows a quadratic equation (curve equation) where the curvature depends on the statistics of the estimated symbols and the SNR. That is not the case with the conventional detector, where the boundaries follow a first order equation (linear equation). On the other hand, investigating the pair-wise boundaries between the regions will be exploited in the SER analysis by considering the pair-wise error probability in Section IV-B.

B. PAIR-WISE ERROR PROBABILITY

In this section, we provide the upper bound on the SER analysis with the pair-wise error probability for the two symbols constellation s_{pw}. The overall SER, given that s_w is transmitted, is calculated as

$$\text{SER} = \sum_{w \neq l} \Pr\left(s_{soft} \in \gamma_l | s = s_w\right) \Pr(s_w) \tag{46}$$

$$= \sum_{w \neq l} \Pr(s_w) \int_{\gamma_l} \text{pdf}_{\mathbf{g}}\left(\mathbf{f} - \boldsymbol{\mu}_{s_w}\right) d\mathbf{f} \tag{47}$$

where $\mathbf{g} \in \mathbb{C}^{2 \times 1} \sim \mathcal{N}_2\left([0\ 0]^T, \Sigma_{s_w}\right)$, $\text{pdf}_{\mathbf{g}}$ is the probability density function of the random variable $\mathbf{g}$, $\boldsymbol{\mu}_{s_w} = \left[\Re(\mu_{s_w})\ \Im(\mu_{s_w})\right]^T$, and γ_l refers to the detection regions related to s_l. Computing the conditional error probability, i.e., the integration, in (47) is, in general, an intractable problem. Instead, a tractable upper bound to it can be found for the mean and variance-based detector as

$$\Pr\left(s_{soft} \in \gamma_l | s = s_w\right) \leq \int_{\gamma_l^{(w)}} \text{pdf}_{\mathbf{g}}\left(\mathbf{f} - \boldsymbol{\mu}_{s_w}\right) d\mathbf{f} \tag{48}$$

where in the right hand side, we replace γ_l in the integration in (47) with a superset $\gamma_l^{(w)}$, which is the half-space region. The integration in (48) represents the pair-wise conditional error probability for s_{pw} constellation, i.e., when s_w is transmitted while the estimated symbol s_{soft} is detected in region $\gamma_l^{(w)}$, and is expressed as

$$\Pr\left(s_w \to s_l\right) = \int_{\gamma_l^{(w)}} \text{pdf}_{\mathbf{g}}\left(\mathbf{f} - \boldsymbol{\mu}_{s_w}\right) d\mathbf{f} \tag{49}$$

$$= \Pr\left(\frac{|s_{soft} - \mu_{s_w}|}{\sqrt{\sigma_{s_w}^2}} > \frac{|s_{soft} - \mu_{s_l}|}{\sqrt{\sigma_{s_l}^2}}\right) \tag{50}$$

$$= \Pr\left(\frac{|g|^2}{\sigma_{s_w}^2} > \frac{|g + \mu_{s_w} - \mu_{s_l}|^2}{\sigma_{s_l}^2}\right) \tag{51}$$

$$= \Pr\left(q(g) > 0\right) \tag{52}$$

with

$$q(g) = \left(\frac{1}{\sigma_{s_w}^2} - \frac{1}{\sigma_{s_l}^2}\right)|g|^2 + 2\frac{\Re\left(g\left(\mu_{s_l} - \mu_{s_w}\right)^*\right)}{\sigma_{s_l}^2} - \frac{|\mu_{s_l} - \mu_{s_w}|^2}{\sigma_{s_l}^2} \tag{53}$$

where (50) is obtained by considering the mean and variance-based detection metric (35), whereas (51) is obtained by

putting $s_{\text{soft}} = g + \mu_{s_w}$, $\mathbf{g} = \left[\Re(g) \ \Im(g) \right]^T$. We can rewrite (53) as

$$q(\mathbf{g}) = \mathbf{g}^T \mathbf{Q}_2 \mathbf{g} + \mathbf{q}_1^T \mathbf{g} + q_0 \qquad (54)$$

and

$$\mathbf{Q}_2 = \left(\frac{1}{\sigma_{s_w}^2} - \frac{1}{\sigma_{s_l}^2} \right) \mathbf{I}_2, \qquad (55)$$

$$\mathbf{q}_1 = \frac{2}{\sigma_{s_l}^2} \left[\left(\Re(\mu_{s_l}) - \Re(\mu_{s_w}) \right) \ \left(\Im(\mu_{s_l}) - \Im(\mu_{s_w}) \right) \right]^T, \qquad (56)$$

$$q_0 = -\frac{|\mu_{s_l} - \mu_{s_w}|^2}{\sigma_{s_l}^2}. \qquad (57)$$

Then, the upper bound on the SER is expressed as

$$\text{SER}_{\text{UB}} = \frac{1}{K} \sum_{w \neq l} \Pr \left(q(\mathbf{g}) > 0 \right). \qquad (58)$$

Through the numerical results, it will be shown that the obtained upper bound is tight, which enables us to utilize the above upper bound to design the transmit constellation symbols in Section V.

C. NUMERICAL RESULTS

In this section, we provide the numerical evaluation of the detection boundaries and the upper bound on the SER analysis introduced in Sections IV-A and IV-B, respectively. Throughout this section, we assume $M = 100$ and $P = 256$, where the pilot sequence is designed as a repetition of the typical 16-QAM constellation. The numerical results are obtained by averaging over 10^5 independent channel realizations and considering the mean and variance-based symbol detector. Unless otherwise stated, the results are obtained through the theoretical analysis presented in Section III-A.

In Figure 11, we verify the detection boundary provided in Theorem 3 between two regions $\gamma_l^{(w)}$ and $\gamma_w^{(l)}$. Firstly, to obtain the boundary by simulations, the pair-wise detector in (35) is applied to all points in the targeted I-Q plane, i.e., using grid search with a step size equal to 0.01 to obtain the pair-wise detection regions (red and green areas). While the theoretical detection boundary ϖ_{lw} (black dashed line) is obtained from (41). Figures 11(a) and (b) show the boundaries between regions with $l = 1, w = 2$ for 0 dB and 20 dB, respectively, while Figures 11(d) and (c) are for the boundaries between regions with $l = 2, w = 4$. The aforementioned figures emphasize that the boundary between two regions depends on the statistics of the estimated symbols and the SNR.

Figure 12 compares the upper bound on the SER with the conventional SER and the SER obtained from the pair-wise detector. The conventional SER is calculated numerically from (47) and based on (29), while the pair-wise detector SER (Pair-Wise Det. SER) is obtained from (35). The upper bound on the SER (SER$_{\text{UB}}$) is obtained from (58), where the probability term is calculated through the ray-tracing method introduced in [42]. The result illustrated in Figure 12 shows

that the pair-wise error probability tightly approximates the actual SER obtained by the Monte Carlo simulations.

V. TRANSMIT CONSTELLATION SYMBOLS DESIGN

As shown in Section III-C, the investigated symbol detectors induced a noticeable improvement in the SIMO system performance in presence of 1-bit ADCs. However, still there is an increasing trend in the SER in the high SNR region. Figure 2(b) indicates that the estimated symbols from different transmit symbols may be close to each other, which inherently increases the SER in the high SNR region. This fact implies that designing appropriate transmit constellation symbols is essential.

In this section, the low-complexity transmit constellation (s) design is proposed as follows. For the design metric, the upper bound on the SER in (58) is used. A straightforward approach is to use a brute force search in the targeted I-Q plane with grid size Δ, although this may be characterized by significant complexity.

Let $\mathbf{S}_{\text{all}}$ denote a set of the all possible constellation $\mathbf{s}$ in the targeted I-Q plane. Both the proposed approach and the brute force search require constructing $\mathbf{S}_{\text{all}}$. The constellation $\mathbf{s}$ is constructed considering a grid step size $\Delta = 0.1$ according to the following conditions:

$$\frac{1}{16} \sum_{l=1}^{16} |s_l|^2 = 1, \qquad (59)$$

$$|s_l|^2 > 0, \quad \forall l, \qquad (60)$$

$$s_l \neq s_w, \quad \forall l \neq w, \qquad (61)$$

$$s_3 = |s_2| \exp\left(j \left(\frac{2\pi}{3} - \angle s_2 \right) \right) \qquad (62)$$

where s_2 and s_3 are related in the same way as in the typical 16-QAM constellation (i.e., as in Figure 2), and the symbols in the other three quadrants are obtained via simple rotation.

In the proposed method, we employ an alternative metric defined as

$$D(s_w, s_l) = \frac{|\mu_{s_w} - \mu_{s_l}|}{\sqrt{\sigma_{s_w}^2 + \sigma_{s_w}^2}} \qquad (63)$$

which indicates the distance between two constellation points s_w and s_l, i.e., $s_w, s_l \in \mathbf{s}$ and $l \neq w$, and this metric is also used in signal detection problems as deflection coefficient. The computational cost of this metric is significantly lower than that of SER$_{\text{UB}}$, as the latter requires numerical integrals in (58) [42].

We also define the minimum metric for constellation $\mathbf{s}$ as

$$D_{\text{min}}(\mathbf{s}) = \min_{s_w, s_l \in \mathbf{s}, \, w \neq l} (D(s_w, s_l)) \qquad (64)$$

and the maximum $D_{\text{min}}(\mathbf{s})$ is given by

$$D_{\text{max}} = \max_{\mathbf{s} \in \mathbf{S}_{\text{all}}} (D_{\text{min}}(\mathbf{s})). \qquad (65)$$

The metric $D(s_w, s_l)$ is used to narrow the candidates of $\mathbf{s}$ and the set of the selected constellations $\mathbf{S}$ is obtained by

$$\mathbf{S} = \{\mathbf{s} | D_{\text{min}}(\mathbf{s}) > \alpha D_{\text{max}}\} \qquad (66)$$

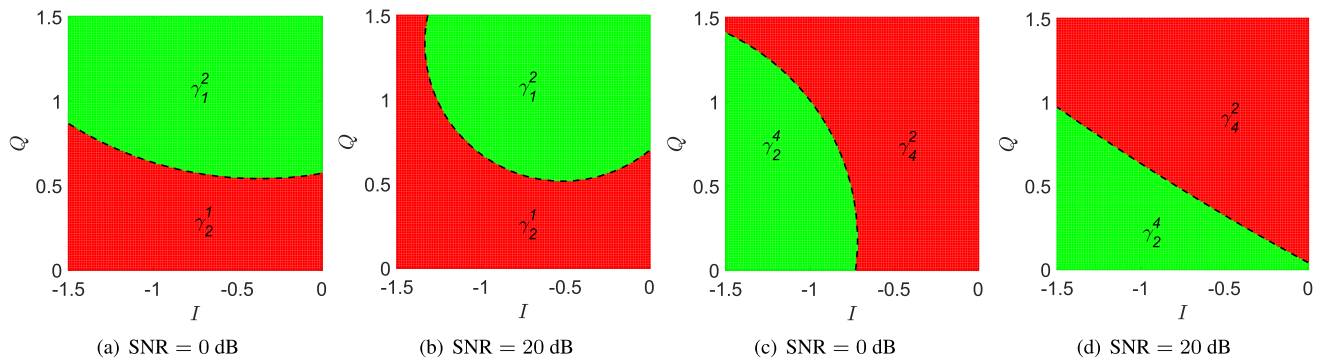(a) SNR = 0 dB (b) SNR = 20 dB (c) SNR = 0 dB (d) SNR = 20 dB

FIGURE 11. The boundary between two regions in the I-Q plane, with $P = 256$ and $M = 100$.
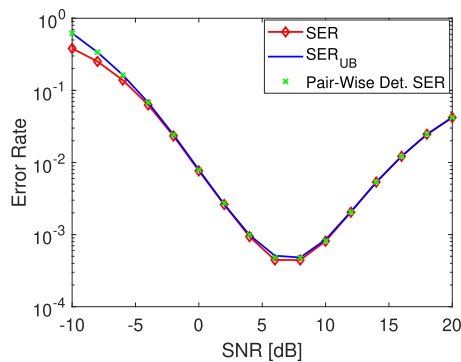

FIGURE 12. Error rate versus the SNR, with $P = 256$ and $M = 100$.
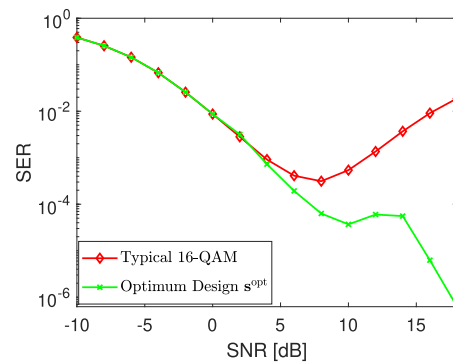

FIGURE 13. SER versus the SNR, with $P = 256$ and $M = 100$.

where α is a ratio as $0 < \alpha < 1$. Finally, in the proposed algorithm, the optimum $\mathbf{s}$ is selected as

$$\mathbf{s}^{\text{opt}} = \min_{\mathbf{s} \in \mathbf{S}} (\text{SER}_{\text{UB}}). \qquad (67)$$

In the case of brute force search, the optimum $\mathbf{s}$ is selected as

$$\mathbf{s}^{\text{opt}} = \underset{\mathbf{s} \in \mathbf{S}_{\text{all}}}{\arg\min} (\text{SER}_{\text{UB}}). \qquad (68)$$

A. NUMERICAL RESULTS

The following setup is considered throughout the section except if something else is mentioned. The numerical results are obtained using the analytical statistics investigated in Section III-A. The pilot sequence is chosen as a repetition of the designed constellation ($\mathbf{s}^{\text{opt}}$), which is transmitted in the data transmission phase with $P = 256$. At the receiver, the mean and variance-based detector is employed and the number of antennas is set to $M = 100$.

Figure 13 illustrates the SER performance comparison between the typical square 16-QAM for $\mathbf{s}$ and the optimum transmit symbol $\mathbf{s}^{\text{opt}}$ obtained from (67). The results show that the optimum transmit symbol exhibits a notable improvement in the SER performance compared with the conventional 16-QAM constellation in the high SNR region. At 12, the SER slightly increases and this behavior is due to the limitation of the grid size. Lastly, the provided results

emphasize that the proposed detectors and the theoretical analysis obtained in Section III are applicable to any constellation design.

Figure 14 shows the distribution of the estimated symbols in the I-Q plane. Figures 14(a)–(c) plot the estimated symbols with the optimum transmit symbols for 4, 10, and 18 dB, respectively. Figures 14(d)–(f) plot the estimated symbols with the typical 16-QAM for 4, 10, and 18 dB, respectively. In this plot, the black cross refer to the transmit symbols, while the red points refer to the distribution of the MRC estimated symbols for the optimum design and the typical 16-QAM in different SNRs. The optimum transmit symbol design depends on the SNR levels.

In the case of the typical square 16-QAM symbols, the estimated symbols of two transmit symbols, which have the same phase, such as $\pi/4$, are getting closer as the SNR increases and they are overlapping at 18 dB as shown in Figure 14(f). This is the problem of the typical square 16-QAM symbols and it causes degraded SER performances in the high SNR region. For this problem, each transmit symbol has a different phase in the optimum transmit symbol design. In addition, the amplitude level for the transmit symbols is also adjusted to avoid the overlapping in Figure 14(c).

In terms of the complexity of the proposed transmit constellation design and the brute force search, the process to construct $\mathbf{S}_{\text{all}}$ is a common part. In the proposed method, the process in (64)–(66) is an additional process compared
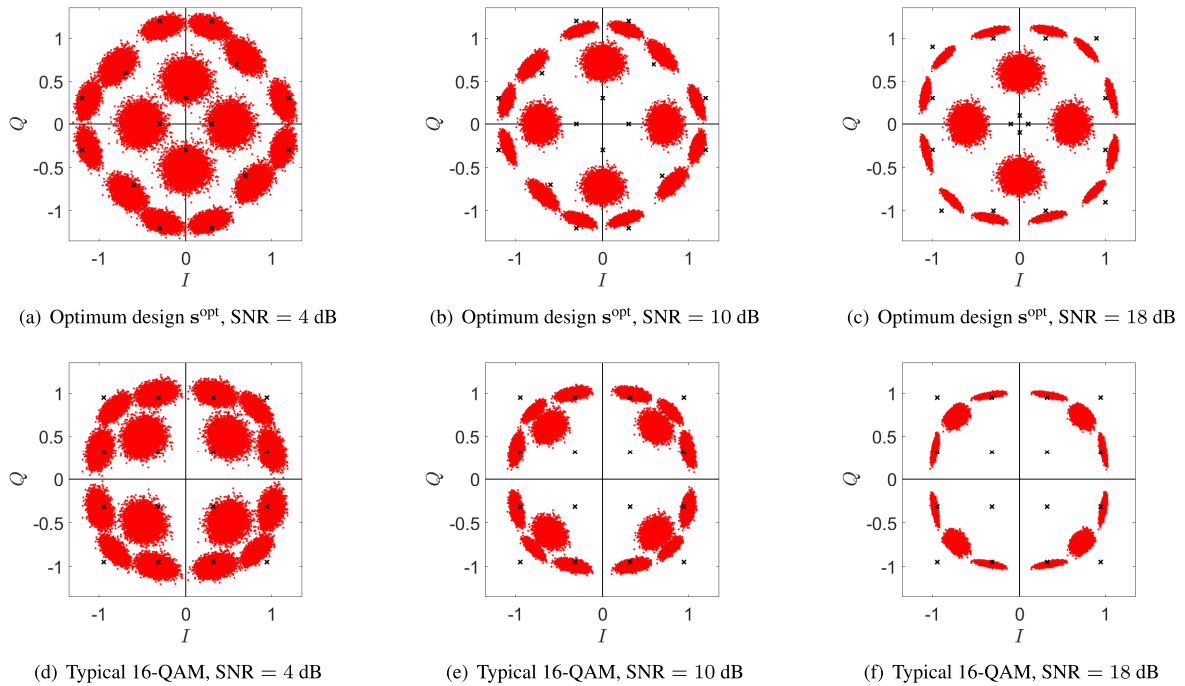
(a) Optimum design $\mathbf{s}^{\mathrm{opt}}$, SNR = 4 dB

(b) Optimum design $\mathbf{s}^{\mathrm{opt}}$, SNR = 10 dB

(c) Optimum design $\mathbf{s}^{\mathrm{opt}}$, SNR = 18 dB

(d) Typical 16-QAM, SNR = 4 dB

(e) Typical 16-QAM, SNR = 10 dB

(f) Typical 16-QAM, SNR = 18 dB

FIGURE 14. Estimated symbols distribution in the I-Q plane, with $P = 256$ and $M = 100$.

TABLE 1. Comparison of the execution times.

	Brute force	Proposed scheme
(63)–(66)	-	~ 0.82821 s
$\min_{\mathbf{s}} (\mathrm{SER_{UB}})$	$\sim 58 \times |\mathbf{S}_{\mathrm{all}}|$ s	$\sim 58 \times |\mathbf{S}|$ s

to the brute force search. On the other hand, the number of computations required for $\mathrm{SER_{UB}}$ in the proposed method and the brute force search are equivalent to the sizes of $\mathbf{S}$ and $\mathbf{S}_{\mathrm{all}}$, respectively. In Table 1, the execution time comparison between the brute force and the proposed scheme is summarized. As shown in the table, the execution time for the additional process in (63)–(66) is about 0.8 s. On the other hand, the execution time for calculating the upper bound on the SER for one candidate of $\mathbf{s}$ is about 58 s and this is significantly larger than the execution time for the additional process. The execution times of optimization for the brute force search and the proposed scheme are proportional to the number of candidates $\mathbf{s}$. These numbers are in fact $|\mathbf{S}_{\mathrm{all}}|$ and $|\mathbf{S}|$ in the brute force search and the proposed scheme, respectively. In case of $\Delta = 0.1$, $|\mathbf{S}_{\mathrm{all}}| \simeq 15000$ for the brute force search, but in the proposed scheme $|\mathbf{S}| \simeq 500$ with SNR = 10 dB and $\alpha = 0.75$. This result indicates that the proposed scheme can reduce the complexity significantly.

VI. CONCLUSION

This paper studies the transmit constellation and received signal detector design for massive SIMO systems with 1-bit ADCs at the BS. First, the statistical analysis of the estimated symbols, i.e., mean and covariance and/or correlation matrix,

for the arbitrary transmit symbols is obtained considering a simple linear estimation, i.e., LS channel estimation and MRC soft symbol estimator. The numerical investigations show that the statistics in the case of 1-bit ADC are totally different from the statistics for high-resolution ADC. We also propose three symbol detectors, in which different statistics are considered. In the simplest symbol detector, only the mean is used, and the second symbol detector utilizes the mean and variance. Finally, the third symbol detector uses the mean, variance and correlation, i.e., covariance matrix between real and imaginary parts of the estimated symbols. The numerical investigations show that the proposed symbol detectors can improve the SER performance by considering the statistics. In addition, we analyze the SER and give the tight upper on the SER as well as the detection boundaries between the detection regions. Finally, we proposed the low-complexity transmit constellation symbols design approach based on the upper bound on the SER criterion. The numerical investigations show that combining the transmit constellation design and received signal detector can improve the SER performance significantly. Specifically, the transmit constellation design can provide the benefit in the high SNR region. In addition, the computational complexity can be reduced to 1/30 by the low-complexity transmit constellation design approach compared to the brute force search.

APPENDIX A
PROOF OF THEOREM 1

From (10), the mean of s_{soft} follows the mean of the ratio distribution. Here, we approximate the mean of the ratio by considering the first order Taylor expansion

approximation [43], [44], [45], and it is approximated as

$$\mathbb{E}\left[c\frac{X}{Y}\right] \approx c\frac{\mathbb{E}[X]}{\mathbb{E}[Y]}. \tag{69}$$

Applying (69) to (10), the mean of s_{soft} can be written as

$$\mathbb{E}[s_{\text{soft}}] \approx P\frac{\mathbb{E}\left[\mathbf{x}\mathbf{R}_{\text{P}}^H\mathbf{r}_{\text{d}}\right]}{\mathbb{E}\left[\mathbf{x}\mathbf{R}_{\text{P}}^H\mathbf{R}_{\text{P}}\mathbf{x}^H\right]}. \tag{70}$$

Building on [34], we define

$$\mathbb{E}\left[\operatorname{sgn}\left(\Re\left(f(x)\right)\right)\operatorname{sgn}\left(\Re\left(f(y)\right)\right)\right] = \Omega\left(\rho_{\text{RR}}^{(x,y)}\right), \tag{71}$$

$$\mathbb{E}\left[\operatorname{sgn}\left(\Im\left(f(x)\right)\right)\operatorname{sgn}\left(\Im\left(f(y)\right)\right)\right] = \Omega\left(\rho_{\text{II}}^{(x,y)}\right) \tag{72}$$

with $f(a) \sim \mathcal{CN}(0, \mathbf{I}_2)$ and $a \in \mathbb{C}$, and where $\rho_{\text{RR}}^{(x,y)}$ and $\rho_{\text{II}}^{(x,y)}$ denote the correlation between $\Re(f(x))$ and $\Re(f(y))$ and between $\Im(f(x))$ and $\Im(f(y))$, respectively, with

$$\rho_{\text{RR}}^{(x,y)} = \rho_{\text{II}}^{(x,y)}. \tag{73}$$

Similarly, we have

$$\mathbb{E}\left[\operatorname{sgn}\left(\Re\left(f(x)\right)\right)\operatorname{sgn}\left(\Im\left(f(y)\right)\right)\right] = \Omega\left(\rho_{\text{RI}}^{(x,y)}\right), \tag{74}$$

$$\mathbb{E}\left[\operatorname{sgn}\left(\Im\left(f(x)\right)\right)\operatorname{sgn}\left(\Re\left(f(y)\right)\right)\right] = \Omega\left(\rho_{\text{IR}}^{(x,y)}\right) \tag{75}$$

with

$$\rho_{\text{RI}}^{(x,y)} = -\rho_{\text{IR}}^{(x,y)}. \tag{76}$$

Let the quantized received data at antenna m be rewritten as

$$r_{\text{d}_m} = \dot{a}_m + j\dot{b}_m \tag{77}$$

and the quantized received pilot p at antenna m as

$$r_{\text{P}_{m,p}} = \ddot{a}_{m,p} + j\ddot{b}_{m,p}. \tag{78}$$

Now, the numerator of s_{soft} in (10) can be expressed as

$$\mathbf{x}\mathbf{R}_{\text{P}}^H\mathbf{r}_{\text{d}} = \sum_{m=1}^M \sum_{p=1}^P \Bigg(x_p\left(\ddot{a}_{m,p}\dot{a}_m + \ddot{b}_{m,p}\dot{b}_m\right) \tag{79}$$

$$+ j\,x_p\left(\ddot{a}_{m,p}\dot{b}_m - \ddot{b}_{m,p}\dot{a}_m\right)\Bigg). \tag{80}$$

From (71)–(76), the mean of $\mathbf{x}\mathbf{R}_{\text{P}}^H\mathbf{r}_{\text{d}}$ can be expressed as

$$\mathbb{E}[\mathbf{x}\mathbf{R}_{\text{P}}^H\mathbf{r}_{\text{d}}] = 2M\sum_{p=1}^P x_p\left(\Omega\left(\rho_{\text{RR}}^{(x_p,s)}\right) + j\,\Omega\left(\rho_{\text{RI}}^{(x_p,s)}\right)\right) \tag{81}$$

where

$$\mathbb{E}[\ddot{a}_{m,p}\dot{a}_m] = \mathbb{E}[\ddot{b}_{m,p}\dot{b}_m] = \Omega\left(\rho_{\text{RR}}^{(x_p,s)}\right), \tag{82}$$

$$\mathbb{E}[\ddot{a}_{m,p}\dot{b}_m] = -\mathbb{E}[\ddot{b}_{m,p}\dot{a}_m] = \Omega\left(\rho_{\text{RI}}^{(x_p,s)}\right). \tag{83}$$

In a similar manner, the denominator of s_{soft} in (10) can be expressed as

$$\mathbf{x}\mathbf{R}_{\text{P}}^H\mathbf{R}_{\text{P}}\mathbf{x}^H = \sum_{p,u=1}^P \sum_{m=1}^M \Bigg(x_p x_u^*\left(\ddot{a}_{m,p}\ddot{a}_{m,u} + \ddot{b}_{m,p}\ddot{b}_{m,u}\right)$$

$$+ j\,x_p x_u^*\left(\ddot{a}_{m,p}\ddot{b}_{m,u} - \ddot{b}_{m,p}\ddot{a}_{m,u}\right)\Bigg) \tag{84}$$

and $E = \mathbb{E}[\mathbf{x}\mathbf{R}_{\text{P}}^H\mathbf{R}_{\text{P}}\mathbf{x}^H]$ can be expressed as

$$E = 2M\Bigg(P + \sum_{u\neq p} x_p x_u^*\bigg(\Omega\left(\rho_{\text{RR}}^{(x_p,x_u)}\right)$$

$$+ j\,\Omega\left(\rho_{\text{RI}}^{(x_p,x_u)}\right)\bigg)\Bigg). \tag{85}$$

By substituting (80) and (85) into (70), the result in Theorem 1 (11) is obtained. ∎

APPENDIX B
PROOF OF THEOREM 2

Considering the estimated symbol s_{soft} in (10) and the approximation assumed in Theorem 1 (69), the variance of the real and imaginary parts of s_{soft} can be written, respectively, as

$$\sigma_{\text{R}_s}^2 = P^2\frac{\mathbb{E}\left[\Re(\mathbf{x}\mathbf{R}_{\text{P}}^H\mathbf{r}_{\text{d}})^2\right]}{\mathbb{E}\left[\left(\mathbf{x}\mathbf{R}_{\text{P}}^H\mathbf{R}_{\text{P}}\mathbf{x}^H\right)^2\right]} - \mu_{\text{R}_s}^2, \tag{86}$$

$$\sigma_{\text{I}_s}^2 = P^2\frac{\mathbb{E}\left[\Im(\mathbf{x}\mathbf{R}_{\text{P}}^H\mathbf{r}_{\text{d}})^2\right]}{\mathbb{E}\left[\left(\mathbf{x}\mathbf{R}_{\text{P}}^H\mathbf{R}_{\text{P}}\mathbf{x}^H\right)^2\right]} - \mu_{\text{I}_s}^2 \tag{87}$$

while the covariance between the real and imaginary parts of the estimated symbol s_{soft} is expressed as

$$\sigma_{\text{RI}_s}^2 = P^2\frac{\mathbb{E}\left[\Re\left(\mathbf{x}\mathbf{R}_{\text{P}}^H\mathbf{r}_{\text{d}}\right)\Im\left(\mathbf{x}\mathbf{R}_{\text{P}}^H\mathbf{r}_{\text{d}}\right)\right]}{\mathbb{E}\left[\left(\mathbf{x}\mathbf{R}_{\text{P}}^H\mathbf{R}_{\text{P}}\mathbf{x}^H\right)^2\right]} - \mu_{\text{R}_s}\mu_{\text{I}_s}. \tag{88}$$

We now present the derivations of the individual terms of (86)–(88) in order. From Theorem 1, we can write μ_{R_s} and μ_{I_s} as

$$\mu_{\text{R}_s} = \frac{2MP}{E}\sum_{p=1}^P\bigg(\Re(x_p)\Omega\left(\rho_{\text{RR}}^{(s,x_p)}\right) \tag{89}$$

$$+ \Im(x_p)\Omega\left(\rho_{\text{RI}}^{(s,x_p)}\right)\bigg), \tag{90}$$

$$\mu_{\text{I}_s} = \frac{2MP}{E}\sum_{p=1}^P\bigg(\Im(x_p)\Omega\left(\rho_{\text{RR}}^{(s,x_p)}\right) \tag{91}$$

$$- \Re(x_p)\Omega\left(\rho_{\text{RI}}^{(s,x_p)}\right)\bigg) \tag{92}$$

respectively. By applying

$$\left(\sum_{m=1}^M\sum_{p=1}^P z_{m,p}\right)^2 = \sum_{m=1}^M\sum_{p=1}^P z_{m,p}^2 + \sum_{m=1}^M\sum_{p\neq u}^P z_{m,p}z_{m,u}$$

$$+ \sum_{m\neq n}\sum_{p=1}^P\sum_{u=1}^P z_{m,p}z_{n,u} \tag{93}$$

to write the square of the real part of (80), we obtain $\chi_R^2 = \Re(\mathbf{xR}_P^H \mathbf{r}_d)^2$ in (95), as shown at the bottom of the page. Then, considering (71)–(76), the mean of χ_R^2 can be expressed as in (96), shown at the bottom of the page. The function $\mathcal{E}(\cdot)$ in (97), as shown at the bottom of the page, denotes the mean of a quadrivariate normally distributed random variable with correlation matrix

$$\mathbf{R} = \begin{bmatrix} 1 & \rho_{RI}^{(s,s)} & \rho_{RR}^{(s,x_p)} & \rho_{RI}^{(s,x_p)} \\ \cdot & 1 & \rho_{IR}^{(s,x_p)} & \rho_{RR}^{(s,x_p)} \\ \cdot & \cdot & 1 & \rho_{RI}^{(x_p,x_p)} \\ \cdot & \cdot & \cdot & 1 \end{bmatrix}. \tag{94}$$

We note that $\mathcal{E}(\cdot)$, which is a function of the correlation matrix R only, is computed numerically since the approximated formulas in the literature are for special case that are not applicable here. As consequence of assuming i.i.d. Rayleigh fading, we have that $\mathbb{E}\left[\dot{b}_m \ddot{a}_{m,p} \dot{b}_n \ddot{a}_{n,u}\right] = \mathbb{E}\left[\dot{b}_m \ddot{a}_{m,p}\right] \mathbb{E}\left[\dot{b}_n \ddot{a}_{n,u}\right]$ if and only if $m \neq n$ regardless of the pilot index p, u. In a similar manner, we can find the expressions of $\mathbb{E}\left[\Im(\mathbf{xR}_P^H \mathbf{r}_d)^2\right]$, $\mathbb{E}\left[\Re(\mathbf{xR}_P^H \mathbf{r}_d)\Im(\mathbf{xR}_P^H \mathbf{r}_d)\right]$, and $\Xi = \mathbb{E}\left[\left(xR_P^H R_P x^H\right)^2\right]$. Finally, Theorem 2 can be obtained by plugging these expressions into (86)–(88). ∎

APPENDIX C
PROOF OF COROLLARY 1
The estimated symbol in (8) can be rewritten as

$$s_{\text{soft}} = \sum_{m=1}^{M} \Re\left(\frac{\hat{h}_m^* r_m}{|h_m|^2}\right) + j\Im\left(\frac{\hat{h}_m^* r_m}{|h_m|^2}\right). \tag{104}$$

$$\chi_R^2 = 2MP + 2\sum_{p=1}^{P}\sum_{m=1}^{M}\left(\Re(x_p)^2 - \Im(x_p)^2\right)\left(\dot{a}_m \dot{b}_m \ddot{a}_{m,p} \ddot{b}_{m,p}\right)$$

$$+ \sum_{p \neq u}\sum_{m=1}^{M}\left(\Re(x_p x_u)\left(\dot{a}_m \dot{b}_m \ddot{a}_{m,p} \ddot{b}_{m,u} + \dot{a}_m \dot{b}_m \ddot{b}_{m,p} \ddot{a}_{m,u}\right) + \Re(x_p^* x_u)\left(\ddot{a}_{m,p} \ddot{a}_{m,u} + \ddot{b}_{m,p} \ddot{b}_{m,u}\right)\right)$$

$$+ \sum_{p \neq u}\sum_{m=1}^{M}\left(\Im(x_p x_u)\left(\dot{a}_m \dot{b}_m \ddot{b}_{m,p} \ddot{b}_{m,u} - \dot{a}_m \dot{b}_m \ddot{a}_{m,p} \ddot{a}_{m,u}\right) + \Im(x_p^* x_u)\left(\ddot{a}_{m,p} \ddot{b}_{m,u} - \ddot{b}_{m,p} \ddot{a}_{m,u}\right)\right)$$

$$+ \sum_{p,u=1}^{P}\sum_{m \neq n}\Re(x_p)\Re(x_u)\left(\dot{a}_m \ddot{a}_{m,p} \dot{a}_n \ddot{a}_{n,u} + \dot{a}_m \ddot{a}_{m,p} \dot{b}_n \ddot{b}_{n,u} + \dot{b}_m \ddot{b}_{m,p} \dot{a}_n \ddot{a}_{n,u} + \dot{b}_m \ddot{b}_{m,p} \dot{b}_n \ddot{b}_{n,u}\right)$$

$$+ \sum_{p,u=1}^{P}\sum_{m \neq n}\Re(x_p)\Im(x_u)\left(\dot{a}_m \ddot{a}_{m,p} \dot{a}_n \ddot{b}_{n,u} - \dot{a}_m \ddot{a}_{m,p} \dot{b}_n \ddot{a}_{n,u} + \dot{b}_m \ddot{b}_{m,p} \dot{a}_n \ddot{b}_{n,u} - \dot{b}_m \ddot{b}_{m,p} \dot{b}_n \ddot{a}_{n,u}\right)$$

$$+ \sum_{p,u=1}^{P}\sum_{m \neq n}\Im(x_p)\Re(x_u)\left(\dot{a}_m \ddot{b}_{m,p} \dot{a}_n \ddot{a}_{n,u} + \dot{a}_m \ddot{b}_{m,p} \dot{b}_n \ddot{b}_{n,u} - \dot{b}_m \ddot{a}_{m,p} \dot{a}_n \ddot{a}_{n,u} - \dot{b}_m \ddot{a}_{m,p} \dot{b}_n \ddot{b}_{n,u}\right)$$

$$+ \sum_{p,u=1}^{P}\sum_{m \neq n}\Im(x_p)\Im(x_u)\left(\dot{a}_m \ddot{b}_{m,p} \dot{a}_n \ddot{b}_{n,u} - \dot{a}_m \ddot{b}_{m,p} \dot{b}_n \ddot{a}_{n,u} - \dot{b}_m \ddot{a}_{m,p} \dot{a}_n \ddot{b}_{n,u} + \dot{b}_m \ddot{a}_{m,p} \dot{b}_n \ddot{a}_{n,u}\right), \tag{95}$$

$$\mathbb{E}[\chi_R^2] = 2MP + 2M\sum_{p=1}^{P}\left(\Re(x_p)^2 - \Im(x_p)^2\right)\mathcal{E}\left(\rho_{RI}^{(s,s)}, \rho_{RR}^{(s,x_p)}, \rho_{RI}^{(s,x_p)}, \rho_{IR}^{(s,x_p)}, \rho_{RR}^{(s,x_p)}, \rho_{RI}^{(x_p,x_p)}\right)$$

$$+ 4M(M-1)\sum_{p,u=1}^{P}\left(\Re(x_p)\Re(x_u)\Omega\left(\rho_{RR}^{(s,x_p)}\right)\Omega\left(\rho_{RR}^{(s,x_u)}\right) + \Re(x_p)\Im(x_u)\Omega\left(\rho_{RR}^{(s,x_p)}\right)\Omega\left(\rho_{RI}^{(s,x_u)}\right)\right)$$

$$+ 4M(M-1)\sum_{p,u=1}^{P}\left(\Im(x_p)\Re(x_u)\Omega\left(\rho_{RI}^{(s,x_p)}\right)\Omega\left(\rho_{RR}^{(s,x_u)}\right) + \Im(x_p)\Im(x_u)\Omega\left(\rho_{RI}^{(s,x_p)}\right)\Omega\left(\rho_{RI}^{(s,x_u)}\right)\right)$$

$$+ M\sum_{p \neq u}\left(2\Re(x_p^* x_u)\Omega\left(\rho_{RR}^{(x_p,x_u)}\right) + \Re(x_p x_u)\mathcal{E}\left(\rho_{RI}^{(s,s)}, \rho_{RR}^{(s,x_p)}, \rho_{RI}^{(s,x_u)}, \rho_{IR}^{(s,x_p)}, \rho_{RR}^{(s,x_u)}, \rho_{RI}^{(x_p,x_u)}\right)\right)$$

$$+ M\sum_{p \neq u}\left(2\Im(x_p^* x_u)\Omega\left(\rho_{RI}^{(x_p,x_u)}\right) + \Re(x_p x_u)\mathcal{E}\left(\rho_{RI}^{(s,s)}, \rho_{RI}^{(s,x_p)}, \rho_{RR}^{(s,x_u)}, \rho_{RR}^{(s,x_p)}, \rho_{IR}^{(s,x_u)}, \rho_{IR}^{(x_p,x_u)}\right)\right)$$

$$+ M\sum_{p \neq u}\Im(x_p x_u)\mathcal{E}\left(\rho_{RI}^{(s,s)}, \rho_{RI}^{(s,x_p)}, \rho_{RI}^{(s,x_u)}, \rho_{RR}^{(s,x_p)}, \rho_{RR}^{(s,x_u)}, \rho_{RR}^{(x_p,x_u)}\right)$$

$$- M\sum_{p \neq u}\Im(x_p x_u)\mathcal{E}\left(\rho_{RI}^{(s,s)}, \rho_{RR}^{(s,x_p)}, \rho_{RR}^{(s,x_u)}, \rho_{IR}^{(s,x_p)}, \rho_{IR}^{(s,x_u)}, \rho_{RR}^{(x_p,x_u)}\right), \tag{96}$$

$$\mathcal{E}\left(\rho_{RI}^{(s,s)}, \rho_{RR}^{(s,x_p)}, \rho_{RI}^{(s,x_p)}, \rho_{IR}^{(s,x_p)}, \rho_{RR}^{(s,x_p)}, \rho_{RI}^{(x_p,x_p)}\right) = \mathbb{E}\left[\dot{a}_m \dot{b}_m \ddot{a}_{m,p} \ddot{b}_{m,p}\right] \tag{97}$$

We can write the real part in (104) as

$$\Re(s_{\text{soft}}) = \sum_{m=1}^{M} g_{R_m} + \sum_{m=1}^{M} v_{R_m} \qquad (105)$$

with

$$\mu_{R_s} = \sum_{m=1}^{M} v_{R_m}, \qquad (106)$$

$$g_{R_m} = \Re\left(\frac{\hat{h}_m^* r_m}{|h_m|^2}\right) - v_{R_m} \qquad (107)$$

where g_{R_m} is a zero mean random variable with finite variance $\Upsilon_{R_m}^2$, $\sigma_{R_s}^2 = \sum_{m=1}^{M} \Upsilon_{R_m}^2$, and g_{R_m} and g_{R_n} are independent if $m \neq n$. From the above, the Cramer's central limit theorem [46] can be applied to (105), then, $\Re(s_{\text{soft}})$ is distributed as

$$\lim_{M \to \infty} \Re(s_{\text{soft}}) \sim \mathcal{N}\left(\mu_{R_s}, \sigma_{R_s}^2\right). \qquad (108)$$

Similarly, we have

$$\lim_{M \to \infty} \Im(s_{\text{soft}}) \sim \mathcal{N}\left(\mu_{I_s}, \sigma_{I_s}^2\right). \qquad (109)$$

From (108), (109), and Theorem 2, the distribution in (26) is obtained. ∎

APPENDIX D
PROOF OF THEOREM 3

Consider any point $\overrightarrow{r}$ lies on the boundary ϖ_{lw} separating the regions $\gamma_w^{(l)}$ and $\gamma_l^{(w)}$, where the scaled EDs between $\overrightarrow{r}$ and the two regions, i.e., mean of the dedicated estimated symbols, are equal. By applying in (29), the equal scaled EDs are given by

$$\frac{|\overrightarrow{r} - \mu_{s_l}|}{\sqrt{\sigma_{s_l}^2}} = \frac{|\overrightarrow{r} - \mu_{s_w}|}{\sqrt{\sigma_{s_w}^2}}. \qquad (110)$$

By taking the square of the two terms, (110) can be rewritten as

$$\frac{|\overrightarrow{r}|^2 + |\mu_{s_l}|^2 - 2\Re\left(\overrightarrow{r} \mu_{s_l}^*\right)}{\sigma_{s_l}^2}$$
$$= \frac{|\overrightarrow{r}|^2 + |\mu_{s_w}|^2 - 2\Re\left(\overrightarrow{r} \mu_{s_w}^*\right)}{\sigma_{s_w}^2}. \qquad (111)$$

Then, we can write

$$(\sigma_{s_w}^2 - \sigma_{s_l}^2)|\overrightarrow{r}|^2 - 2\left(\sigma_{s_w}^2 \Re\left(\overrightarrow{r} \mu_{s_l}^*\right) - \sigma_{s_l}^2 \Re\left(\overrightarrow{r} \mu_{s_w}^*\right)\right)$$
$$= \sigma_{s_l}^2 |\mu_{s_w}|^2 - \sigma_{s_w}^2 |\mu_{s_l}|^2. \qquad (112)$$

Finally, the boundary equation in (41) is obtained by considering $\overrightarrow{r} = \dot{x} + j\dot{y}$. ∎

$$\xi_1 = \sum_{p \neq u} \left(\Re(x_p^* x_u) \, \Omega\left(\rho_{RR}^{(x_p, x_u)}\right) + \Im(x_p^* x_u) \, \Omega\left(\rho_{RI}^{(x_p, x_u)}\right)\right), \qquad (98)$$

$$\xi_2 = \sum_{p=1}^{P} \left(\Re(x_p)^2 - \Im(x_p)^2\right) \mathcal{E}\left(\rho_{RI}^{(s,s)}, \rho_{RR}^{(s,x_p)}, \rho_{RI}^{(s,x_p)}, \rho_{IR}^{(s,x_p)}, \rho_{RR}^{(s,x_p)}, \rho_{RI}^{(x_p,x_p)}\right), \qquad (99)$$

$$\xi_3 = \sum_{p \neq u} \Re(x_p x_u)\Big(\mathcal{E}\left(\rho_{RI}^{(s,s)}, \rho_{RR}^{(s,x_p)}, \rho_{RI}^{(s,x_u)}, \rho_{IR}^{(s,x_p)}, \rho_{RR}^{(s,x_u)}, \rho_{RI}^{(x_p,x_u)}\right)$$
$$+ \mathcal{E}\left(\rho_{RI}^{(s,s)}, \rho_{RI}^{(s,x_p)}, \rho_{RR}^{(s,x_u)}, \rho_{RR}^{(s,x_p)}, \rho_{IR}^{(s,x_u)}, \rho_{IR}^{(x_p,x_u)}\right)\Big)$$
$$+ \sum_{p \neq u} \Im(x_p x_u)\Big(\mathcal{E}\left(\rho_{RI}^{(s,s)}, \rho_{RI}^{(s,x_p)}, \rho_{RI}^{(s,x_u)}, \rho_{RR}^{(s,x_p)}, \rho_{RR}^{(s,x_u)}, \rho_{RR}^{(x_p,x_u)}\right)$$
$$- \mathcal{E}\left(\rho_{RI}^{(s,s)}, \rho_{RR}^{(s,x_p)}, \rho_{RR}^{(s,x_u)}, \rho_{IR}^{(s,x_p)}, \rho_{IR}^{(s,x_u)}, \rho_{RR}^{(x_p,x_u)}\right)\Big), \qquad (100)$$

$$\bar{\xi}_1 = \sum_{p \neq u} \left(\Re(x_p^* x_u)\Omega\left(\rho_{IR}^{x_p, x_u}\right) + \Im(x_p^* x_u)\Omega\left(\rho_{RR}^{x_p, x_u}\right)\right), \qquad (101)$$

$$\bar{\xi}_2 = \sum_{p=1}^{P} \Re(x_p)\Im(x_u)\mathcal{E}\left(\rho_{RI}^{(s,s)}, \rho_{RR}^{(s,x_p)}, \rho_{RI}^{(s,x_p)}, \rho_{IR}^{(s,x_p)}, \rho_{RR}^{(s,x_p)}, \rho_{RI}^{(x_p,x_p)}\right), \qquad (102)$$

$$\bar{\xi}_3 = \sum_{p \neq u} \Re(x_p x_u)\Big(\mathcal{E}\left(\rho_{RI}^{(s,s)}, \rho_{RR}^{(s,x_p)}, \rho_{RR}^{(s,x_u)}, \rho_{IR}^{(s,x_p)}, \rho_{IR}^{(s,x_u)}, \rho_{RR}^{(x_p,x_u)}\right)$$
$$- \mathcal{E}\left(\rho_{RI}^{(s,s)}, \rho_{RI}^{(s,x_p)}, \rho_{RI}^{(s,x_u)}, \rho_{RR}^{(s,x_p)}, \rho_{RR}^{(s,x_u)}, \rho_{RR}^{(x_p,x_u)}\right)\Big)$$
$$+ \sum_{p \neq u} \Im(x_p x_u)\Big(\mathcal{E}\left(\rho_{RI}^{(s,s)}, \rho_{RR}^{(s,x_p)}, \rho_{RI}^{(s,x_u)}, \rho_{IR}^{(s,x_p)}, \rho_{RR}^{(s,x_u)}, \rho_{RI}^{(x_p,x_u)}\right)$$
$$+ \mathcal{E}\left(\rho_{RI}^{(s,s)}, \rho_{RI}^{(s,x_p)}, \rho_{RR}^{(s,x_u)}, \rho_{RR}^{(s,x_p)}, \rho_{IR}^{(s,x_u)}, \rho_{IR}^{(x_p,x_u)}\right)\Big) \qquad (103)$$

REFERENCES

[1] R. Dangi, P. Lalwani, G. Choudhary, I. You, and G. Pau, "Study and investigation on 5G technology: A systematic review," *Sensors*, vol. 22, no. 1, p. 26, Dec. 2021.

[2] E. G. Larsson, O. Edfors, F. Tufvesson, and T. L. Marzetta, "Massive MIMO for next generation wireless systems," *IEEE Commun. Mag.*, vol. 52, no. 2, pp. 186–195, Feb. 2014.

[3] R. Chataut and R. Akl, "Massive MIMO systems for 5G and beyond networks—Overview, recent trends, challenges, and future research direction," *Sensors*, vol. 20, no. 10, p. 2753, May 2020.

[4] K. N. R. S. V. Prasad, E. Hossain, and V. K. Bhargava, "Energy efficiency in massive MIMO-based 5G networks: Opportunities and challenges," *IEEE Wireless Commun.*, vol. 24, no. 3, pp. 86–94, Jun. 2017.

[5] J. M. Khoury, "On the design of constant settling time AGC circuits," *IEEE Trans. Circuits Syst. II, Analog Digit. Signal Process.*, vol. 45, no. 3, pp. 283–294, Mar. 1998.

[6] Y. Xiong, Z. Zhang, N. Wei, B. Li, and Y. Chen, "Performance analysis of uplink massive MIMO systems with variable-resolution ADCs using MMSE and MRC detection," *Trans. Emerg. Telecommun. Technol.*, vol. 30, no. 5, p. e3549, Jan. 2019.

[7] A. Mezghani and J. A. Nossek, "On ultra-wideband MIMO systems with 1-bit quantized outputs: Performance analysis and input optimization," in *Proc. IEEE Int. Symp. Inf. Theory*, Jun. 2007, pp. 1286–1289.

[8] C. Mollén, J. Choi, E. G. Larsson, and R. W. Heath Jr., "Uplink performance of wideband massive MIMO with one-bit ADCs," *IEEE Trans. Wireless Commun.*, vol. 16, no. 1, pp. 87–100, Jan. 2017.

[9] S. Gayan, R. Senanayake, H. Inaltekin, and J. Evans, "Reliability characterization for SIMO communication systems with low-resolution phase quantization under Rayleigh fading," *IEEE Open J. Commun. Soc.*, vol. 2, pp. 2660–2679, 2021.

[10] N. I. Bernardo, J. Zhu, and J. Evans, "On minimizing symbol error rate over fading channels with low-resolution quantization," *IEEE Trans. Commun.*, vol. 69, no. 11, pp. 7205–7221, Nov. 2021.

[11] J. Singh, O. Dabeer, and U. Madhow, "On the limits of communication with low-precision analog-to-digital conversion at the receiver," *IEEE Trans. Commun.*, vol. 57, no. 12, pp. 3629–3639, Dec. 2009.

[12] A. Mezghani and J. A. Nossek, "Capacity lower bound of MIMO channels with output quantization and correlated noise," in *Proc. IEEE Int. Symp. Inf. Theory (ISIT)*, Jul. 2012, pp. 1–5.

[13] J. Mo and R. W. Heath Jr., "Capacity analysis of one-bit quantized MIMO systems with transmitter channel state information," *IEEE Trans. Signal Process.*, vol. 63, no. 20, pp. 5498–5512, Oct. 2015.

[14] J. Mo and R. W. Heath Jr., "High SNR capacity of millimeter wave MIMO systems with one-bit quantization," in *Proc. Inf. Theory Appl. Workshop (ITA)*, Feb. 2014, pp. 1–5.

[15] N. I. Bernardo, J. Zhu, Y. C. Eldar, and J. Evans, "Capacity bounds for one-bit MIMO Gaussian channels with analog combining," 2022, *arXiv:2204.04033*.

[16] Y. Li, C. Tao, G. Seco-Granados, A. Mezghani, A. L. Swindlehurst, and L. Liu, "Channel estimation and performance analysis of one-bit massive MIMO systems," *IEEE Trans. Signal Process.*, vol. 65, no. 15, pp. 4075–4089, Apr. 2017.

[17] Z. Shao, L. T. N. Landau, and R. C. D. Lamare, "Channel estimation for large-scale multiple-antenna systems using 1-bit ADCs and oversampling," *IEEE Access*, vol. 8, pp. 85243–85256, 2020.

[18] M. S. Stein, S. Bar, J. A. Nossek, and J. Tabrikian, "Performance analysis for channel estimation with 1-bit ADC and unknown quantization threshold," *IEEE Trans. Signal Process.*, vol. 66, no. 10, pp. 2557–2571, May 2018.

[19] O. Dabeer and U. Madhow, "Channel estimation with low-precision analog-to-digital conversion," in *Proc. ICC*, May 2010, pp. 1–6.

[20] S. S. Thoota and C. R. Murthy, "Massive MIMO-OFDM systems with low resolution ADCs: Cramér-rao bound, sparse channel estimation, and soft symbol decoding," *IEEE Trans. Signal Process.*, vol. 70, pp. 4835–4850, 2022.

[21] R. Zhou, H. Du, and D. Zhang, "Millimeter wave MIMO channel estimation with one-bit receivers," *IEEE Commun. Lett.*, vol. 26, no. 1, pp. 158–162, Jan. 2022.

[22] J. Mo, P. Schniter, and R. W. Heath Jr., "Channel estimation in broadband millimeter wave MIMO systems with few-bit ADCs," *IEEE Trans. Signal Process.*, vol. 66, no. 5, pp. 1141–1154, Mar. 2018.

[23] J. Choi, J. Mo, and R. W. Heath Jr., "Near maximum-likelihood detector and channel estimator for uplink multiuser massive MIMO systems with one-bit ADCs," *IEEE Trans. Commun.*, vol. 64, no. 5, pp. 2005–2018, Mar. 2016.

[24] Y.-S. Jeon, N. Lee, S.-N. Hong, and R. W. Heath Jr., "One-bit sphere decoding for uplink massive MIMO systems with one-bit ADCs," *IEEE Trans. Wireless Commun.*, vol. 17, no. 7, pp. 4509–4521, Jul. 2018.

[25] J.-C. Chen, "One-bit MMSE equalization for all-digital massive MU-MIMO communication systems," *IEEE Syst. J.*, vol. 16, no. 3, pp. 4916–4927, Sep. 2022.

[26] L. Li and J. Hu, "Low-complexity linear massive MIMO detection based on the improved BFGS method," *IET Commun.*, vol. 16, no. 14, pp. 1699–1707, May 2022.

[27] S. Wang, Y. Li, and J. Wang, "Multiuser detection in massive spatial modulation MIMO with low-resolution ADCs," *IEEE Trans. Wireless Commun.*, vol. 14, no. 4, pp. 2156–2168, Apr. 2015.

[28] E. S. P. Lopes and L. T. N. Landau, "Iterative detection and decoding for multiuser MIMO systems with low resolution precoding and PSK modulation," in *Proc. IEEE Stat. Signal Process. Workshop (SSP)*, Jul. 2021, pp. 356–360.

[29] C. Risi, D. Persson, and E. G. Larsson, "Massive MIMO with 1-bit ADC," 2014, *arXiv:1404.7736*.

[30] A. B. Ucuncu and A. O. Yilmaz, "Performance analysis of faster than symbol rate sampling in 1-bit massive MIMO systems," in *Proc. IEEE Int. Conf. Commun. (ICC)*, May 2017, pp. 1–6.

[31] A. B. Üçüncü and A. Ö. Yilmaz, "Oversampling in one-bit quantized massive MIMO systems and performance analysis," *IEEE Trans. Wireless Commun.*, vol. 17, no. 12, pp. 7952–7964, Dec. 2018.

[32] A. B. Ucuncu and A. O. Yilmaz, "Uplink performance analysis of over-sampled wideband massive MIMO with one-bit ADCs," in *Proc. IEEE 88th Veh. Technol. Conf. (VTC-Fall)*, Aug. 2018, pp. 1–5.

[33] S. Jacobsson, G. Durisi, M. Coldrey, U. Gustavsson, and C. Studer, "One-bit massive MIMO: Channel estimation and high-order modulations," in *Proc. IEEE Int. Conf. Commun. Workshop (ICCW)*, Jun. 2015, pp. 1304–1309.

[34] I. Atzeni and A. Tolli, "Channel estimation and data detection analysis of massive MIMO with 1-bit ADCs," *IEEE Trans. Wireless Commun.*, vol. 21, no. 6, pp. 3850–3867, Jun. 2022.

[35] A. Azizzadeh, R. Mohammadkhani, S. V. A.-D. Makki, and E. Björnson, "BER performance analysis of coarsely quantized uplink massive MIMO," *Signal Process.*, vol. 161, pp. 259–267, Aug. 2019.

[36] S. Jacobsson, G. Durisi, M. Coldrey, U. Gustavsson, and C. Studer, "Throughput analysis of massive MIMO uplink with low-resolution ADCs," *IEEE Trans. Wireless Commun.*, vol. 16, no. 6, pp. 4038–4051, Jun. 2017.

[37] L. Liu, Y. Ma, and R. Tafazolli, "MIMO or SIMO for wireless communications with binary-array receivers," in *Proc. IEEE Int. Conf. Commun. Workshops (ICC Workshops)*, Jun. 2020, pp. 1–6.

[38] S. Kay, "Can detectability be improved by adding noise?" *IEEE Signal Process. Lett.*, vol. 7, no. 1, pp. 8–10, Jan. 2000.

[39] A. K. Fletcher, S. Rangan, V. K. Goyal, and K. Ramchandran, "Robust predictive quantization: Analysis and design via convex optimization," *IEEE J. Sel. Topics Signal Process.*, vol. 1, no. 4, pp. 618–632, Dec. 2007.

[40] J. J. Bussgang, "Crosscorrelation functions of amplitude-distorted Gaussian signals," Res. Lab. Electron., Tech. Rep., 216, 1952.

[41] D. Abdelhameed, K. Umebayashi, A. Al-Tahmeesschi, I. Atzeni, and A. Tolli, "Enhanced signal detection for massive SIMO communications with 1-bit ADCs," in *Proc. IEEE 22nd Int. Workshop Signal Process. Adv. Wireless Commun. (SPAWC)*, Sep. 2021, pp. 66–70.

[42] A. Das and W. S. Geisler, "A method to integrate and classify normal distributions," *J. Vis.*, vol. 21, no. 10, p. 1, Sep. 2021.

[43] A. Stuart and J. K. Ord, *Kendall's Advanced Theory of Statistics*, vol. 1, 6th ed. London, U.K.: Arnold, 1998.

[44] R. C. Elandt-Johnson and N. L. Johnson, *Survival Models and Data Analysis*. Hoboken, NJ, USA: Wiley, 1980.

[45] K. M. Wolter, *Introduction to Variance Estimation*. Berlin, Germany: Springer, 2007. [Online]. Available: https://cds.cern.ch/record/1338203

[46] H. Cramer, *Random Variables and Probability Distributions*. Cambridge, U.K.: Cambridge Univ. Press, Jan. 1970.

DOAA ABDELHAMEED (Student Member, IEEE) received the B.Sc. degree (Hons.) in electrical engineering and the M.Sc. degree in communications and electronics from Aswan University, Egypt, in 2012 and 2017, respectively. She is currently pursuing the Ph.D. degree with the Tokyo University of Agriculture and Technology, Japan. Her research interests include massive MIMO technology, 1-bit ADC, channel estimation, and signal detection for wireless communication.

ITALO ATZENI (Member, IEEE) received the M.Sc. degree (Hons.) in telecommunications engineering from the University of Cagliari, Italy, in 2010, and the Ph.D. degree (Hons.) in signal theory and communications from the Polytechnic University of Catalonia (BarcelonaTech), Spain, in 2014. From 2014 to 2017, he was a Researcher with the Mathematical and Algorithmic Sciences Laboratory, Paris Research Center, Huawei Technologies, France. From 2017 to 2018, he was a Research Associate with the Communication Systems Department, EURECOM, France. He previously held a visiting research appointment at The Hong Kong University of Science and Technology, Hong Kong, in 2013. Since 2019, he has been with the Centre for Wireless Communications, University of Oulu, Finland, where he is currently an Assistant Professor and an Academy of Finland Research Fellow, from 2022 to 2027. His primary research interests include communication and information theory, statistical signal processing, convex and distributed optimization theory, and their applications to low-complexity and energy-efficient solutions for multi-antenna communications. He received the Best Paper Award from the Wireless Communications Symposium at IEEE ICC 2019. He serves as an Editor for the IEEE COMMUNICATIONS LETTERS.

KENTA UMEBAYASHI (Member, IEEE) received the L.L.B. degree from Ritsumeikan University, Japan, in 1996, and the B.E., M.E., and Ph.D. degrees from Yokohama National University, Japan, in 1999, 2001, and 2004, respectively. From 2004 to 2006, he was a Research Scientist with the Centre for Wireless Communications, University of Oulu, Finland. He is currently a Professor with the Tokyo University of Agriculture and Technology, Japan. He was a principal investigator of four grants-in-aid for scientific research projects and three strategic information and communications research and development promotion programme projects, including a HORIZON2020 Project. His research interests include signal detection and estimation theories for wireless communication, signal processing for multiple antenna systems, cognitive radio networks, and terahertz band wireless communications. He received the Best Paper Award from the 2012 IEEE WCNC and the 2015 IEEE WCNC International Workshop on Smart Spectrum (IWSS).

ANTTI TÖLLI (Senior Member, IEEE) received the Dr.Sc. (Tech.) degree in electrical engineering from the University of Oulu, Oulu, Finland, in 2008. From 1998 to 2003, he worked with Nokia Networks as a Research Engineer and a Project Manager at Finland and Spain. In May 2014, he was granted a five year (from 2014 to 2019) an Academy Research Fellow position at the Academy of Finland. From 2015 to 2016, he visited at EURECOM, Sophia Antipolis, France. From August 2018 to June 2019, he was visiting at the University of California at Santa Barbara, Santa Barbara, CA, USA. He is currently a Professor with the Centre for Wireless Communications (CWC), University of Oulu. He has authored numerous papers in peer-reviewed international journals and conferences and several patents all in the area of signal processing and wireless communications. His research interests include radio resource management and transceiver design for broadband wireless communications with a special emphasis on distributed interference management in heterogeneous wireless networks. From 2017 to 2021, he served as an Associate Editor for the IEEE TRANSACTIONS ON SIGNAL PROCESSING.

• • •